

GAUGE-INVARIANT FROZEN GAUSSIAN APPROXIMATION METHOD FOR THE SCHRÖDINGER EQUATION WITH PERIODIC POTENTIALS

RICARDO DELGADILLO, JIANFENG LU, AND XU YANG

ABSTRACT. We develop a gauge-invariant frozen Gaussian approximation (GIFGA) method for the linear Schrödinger equation (LSE) with periodic potentials in the semiclassical regime. The method generalizes the Herman-Kluk propagator for LSE to the case with periodic media. It provides an efficient computational tool based on asymptotic analysis on phase space and Bloch waves to capture the high-frequency oscillations of the solution. Compared to geometric optics and Gaussian beam methods, GIFGA works in both scenarios of caustics and beam spreading. Moreover, it is invariant with respect to the gauge choice of the Bloch eigenfunctions, and thus avoids the numerical difficulty of computing gauge-dependent Berry phase. We numerically test the method by several one-dimensional examples, in particular, the first order convergence is validated, which agrees with our companion analysis paper [Delgadillo, Lu and Yang, arXiv:1504.08051].

1. INTRODUCTION

The focus of this work is to develop efficient numerical methods for solving the following semiclassical Schrödinger equation whose potential term consists of a (highly oscillatory) microscopic periodic potential and a macroscopic smooth potential,

$$(1.1) \quad i\varepsilon \frac{\partial \psi^\varepsilon}{\partial t} = -\frac{\varepsilon^2}{2} \Delta \psi^\varepsilon + V_\Gamma \left(\frac{\mathbf{x}}{\varepsilon} \right) \psi^\varepsilon + U(\mathbf{x}) \psi^\varepsilon, \quad \mathbf{x} \in \mathbb{R}^d.$$

Here $\psi^\varepsilon(t, \mathbf{x})$ is the wave function and $\varepsilon \ll 1$ is an effective Planck constant. The equation (1.1) can be viewed as a model for electron dynamics in crystal under the one-particle approximation. The periodic lattice potential V_Γ is generated by the ionic cores and electrons in the crystal, and hence periodic with respect to the lattice \mathbb{L} with unit cell $\Gamma := [-\pi, \pi]^d$. In (1.1), U is a smooth external macroscopic potential, which counts for e.g., external electric field.

Direct numerical simulation of (1.1) is prohibitively expensive due to the small parameter ε in the semiclassical regime. In order to accurately capture the small scale features caused by V_Γ , a mesh size of order $o(\varepsilon)$ is usually required in time and space, e.g., in the standard time-splitting spectral method [1]. If only physical observables (e.g., density, flux and energy) are needed, one can relax the time step requirement to $\mathcal{O}(1)$ with a coarser mesh size of $\mathcal{O}(\varepsilon)$ using the Bloch decomposition based time-splitting spectral method as proposed in [8–10]. However, computation of the solution ψ^ε

Date: October 7, 2018.

R.D. and X.Y. were partially supported by the NSF grants DMS-1418936 and DMS-1107291: NSF Research Network in Mathematical Sciences “Kinetic description of emerging challenges in multiscale problems of natural science”. They also acknowledge support from the Center for Scientific Computing at the CNSI and MRL: an NSF MRSEC (DMR-1121053) and NSF CNS-0960316. The work of J.L. was supported in part by the Alfred P. Sloan Foundation and the National Science Foundation under award DMS-1312659 and DMS-1454939. X.Y. was also partially supported by the Regents Junior Faculty Fellowship and Hellman Family Foundation Faculty Fellowship of University of California, Santa Barbara.

to (1.1) is still very expensive for $\varepsilon \ll 1$, especially in high dimensions. For this reason, alternative approaches based on asymptotic analysis have been developed, among which, the geometric optics (GO) approach is based on the WKB ansatz under the adiabatic approximation,

$$\psi^\varepsilon(t, \mathbf{x}) = a(t, \mathbf{x}) u_n \left(\nabla_{\mathbf{x}} S, \frac{\mathbf{x}}{\varepsilon} \right) e^{iS(t, \mathbf{x})/\varepsilon}.$$

Here $u_n(\boldsymbol{\xi}, \mathbf{x})$ is the Bloch eigenfunction normalized for each $\boldsymbol{\xi} \in \Gamma^* := [0, 1)^d$:

$$(1.2) \quad \int_{\Gamma} |u_n(\boldsymbol{\xi}, \mathbf{x})|^2 d\mathbf{x} = 1,$$

which corresponds to the n -th energy band $E_n(\boldsymbol{\xi})$ (see e.g., [2]):

$$(1.3) \quad H_{\boldsymbol{\xi}} u_n(\boldsymbol{\xi}, \mathbf{x}) = E_n(\boldsymbol{\xi}) u_n(\boldsymbol{\xi}, \mathbf{x}),$$

with the Bloch Hamiltonian

$$(1.4) \quad H_{\boldsymbol{\xi}} := \frac{1}{2} (-i\partial_{\mathbf{x}} + \boldsymbol{\xi})^2 + V_{\Gamma}(\mathbf{x}),$$

and periodic boundary conditions on Γ .

Then GO solves $S(t, \mathbf{x})$ as the solution to an eikonal equation and $\rho(t, \mathbf{x}) = |a(t, \mathbf{x})|^2$ given by a transport equation:

$$(1.5) \quad \partial_t S + E_n(\nabla_{\mathbf{x}} S) + U(\mathbf{x}) = 0,$$

$$(1.6) \quad \partial_t \rho + \nabla_{\mathbf{x}} \cdot (\rho \nabla_{\boldsymbol{\xi}} E_n(\nabla_{\mathbf{x}} S)) = 0.$$

While this method is ε -independent, it breaks down at caustics where the Hamilton-Jacobi equation (1.5) develops singularities.

The Gaussian beam method (GBM) was proposed in [5, 6] to overcome this drawback at caustics, with some recent developments [4, 11–14, 24, 25], which in particular extends the method to periodic media. GBM is based on the single beam solution, which has a similar form as the WKB ansatz

$$\psi^\varepsilon(t, \mathbf{x}) = a(t, \mathbf{y}) u_n \left(\nabla_{\mathbf{x}} S, \frac{\mathbf{x}}{\varepsilon} \right) e^{i\tilde{S}(t, \mathbf{x}, \mathbf{y})/\varepsilon}.$$

The difference lies in that GBM uses a complex phase function,

$$(1.7) \quad \tilde{S}(t, \mathbf{x}, \mathbf{y}) = S(t, \mathbf{y}) + \mathbf{p}(t, \mathbf{y}) \cdot (\mathbf{x} - \mathbf{y}) + \frac{1}{2} (\mathbf{x} - \mathbf{y}) \cdot M(t, \mathbf{y}) (\mathbf{x} - \mathbf{y}),$$

where $S \in \mathbb{R}$, $\mathbf{p} \in \mathbb{R}^d$, $M \in \mathbb{C}^{d \times d}$. The imaginary part of M is chosen to be positive definite so that the solution decays exponentially away from $\mathbf{x} = \mathbf{y}$ as a Gaussian, where \mathbf{y} is called the beam center. If the initial wave is not in a form of single beam, one can approximate it by a superposition of Gaussian beams. The validity of this construction at caustics was analyzed in [4].

The accuracy of GBM relies on the truncation error of the Taylor expansion of \tilde{S} around the beam center \mathbf{y} up to the quadratic term, and thus it loses accuracy when the width of the beam becomes large, i.e., when the imaginary part of $M(t, \mathbf{y})$ in (1.7) becomes small so that the Gaussian function is no longer localized. This happens for example when the solution of the Schrödinger equation spreads (the opposite situation of forming caustics). This is a severe problem in general, as shown in [16, 19, 21]. One can overcome the problem of spreading of beams by doing reinitialization once in a while, see [20, 21], however, this increases the computational complexity especially when beams spread quickly.

In the setting of semiclassical Schrödinger equations with periodic potential, another challenge for asymptotics methods, not emphasized enough in the literature though, comes from the gauge freedom in (1.3). That is, for any Bloch eigenfunction $u_n(\boldsymbol{\xi}, \mathbf{x})$, $u_n(\boldsymbol{\xi}, \mathbf{x}) e^{i\phi(\boldsymbol{\xi})}$ also solves (1.3) for any

arbitrary phase function $\phi(\boldsymbol{\xi})$. In particular, when one solves the Bloch waves numerically from (1.3) for different $\boldsymbol{\xi}$, it is very difficult, if not impossible, to make sure that the phase depends smoothly on $\boldsymbol{\xi}$. The arbitrariness creates difficulty when one needs to get the eigenfunctions off numerical grids by interpolation, e.g., in the Gaussian beam method [4].

In this paper, we develop a gauge-invariant frozen Gaussian approximation (GIFGA) method for the Schrödinger equation with periodic potentials. This method generalizes the Herman-Kluk propagator [7] by including Bloch waves in the integral representation. It provides an efficient computational tool based on asymptotic analysis on phase plane, with a first order accuracy established in our companion analysis paper [3]. It inherits the merits of the frozen Gaussian approximation studied in [16–18], which works in both scenarios of caustics and beam spreading. The formulation is also invariant with respect to the gauge choice of the Bloch eigenfunctions. In particular, we avoid the numerical computation of the Berry phase, which causes difficulty since it depends on the derivatives of Bloch eigenfunctions with respect to crystal momentum, and is hence not always well-defined if an arbitrary gauge choice was made. This is achieved by using a trick inspired by the work of Vanderbilt and King-Smith [15] in the context of modern theory of polarization. The details will be explained in Section 2.3, see in particular, (2.18)–(2.22).

The rest of the paper is organized as follows: In Section 2, we will introduce the GIFGA method. In Section 3, we briefly describe how to numerically compute Bloch eigenvalues and eigenfunctions. We also describe how to numerically implement the GIFGA method described in Section 2. Section 4 presents numerical evidence supporting the initial decomposition described in Section 2 along with examples confirming our analytical results in [3]. The last two examples in Section 4 provides the numerical performance of GIFGA. We make some concluding remarks in Section 5.

2. FORMULATION OF THE FROZEN GAUSSIAN APPROXIMATION

This section is devoted to the development of the gauge-invariant frozen Gaussian approximation (GIFGA) in periodic media based on Bloch decomposition. We first recall the Bloch decomposition for Schrödinger operators with a periodic potential. The Bloch waves will be used to capture the high-frequency oscillatory structure of the solution given by GIFGA. After stating the asymptotic solution, the formulation of which is gauge-invariant, we recall some analytical results on the convergence of GIFGA.

2.1. The Bloch decomposition. Recall that the potential $V_{\Gamma}(\boldsymbol{x})$ in (1.1) is smooth and periodic with respect to the lattice \mathbb{L} with unit cell $\Gamma = [-\pi, \pi)^d$. The unit cell of the reciprocal lattice, known as the first Brillouin zone, is then given by $\Gamma^* = [0, 1)^d$.

The eigenvalues of the self-adjoint Bloch Hamiltonian $H_{\boldsymbol{\xi}}$, defined in (1.4) on $L^2(\Gamma)$ are real and ordered increasingly (counting multiplicity) as

$$(2.1) \quad E_1(\boldsymbol{\xi}) \leq E_2(\boldsymbol{\xi}) \leq \cdots \leq E_n(\boldsymbol{\xi}) \leq \cdots, \quad n \in \mathbb{N}$$

for each $\boldsymbol{\xi} \in \Gamma^*$. Furthermore, the eigenfunctions $\{u_n(\boldsymbol{\xi}, \boldsymbol{x})\}_{n=1}^{\infty}$ for each $\boldsymbol{\xi} \in \Gamma^*$, known as the Bloch waves, form an orthonormal basis of $L^2(\Gamma)$ [2].

We extend $u_n(\boldsymbol{\xi}, \boldsymbol{x})$ periodically with respect to \boldsymbol{x} so that it is defined on all of \mathbb{R}^d , and then the Bloch decomposition is given by, $\forall f \in L^2(\mathbb{R}^d)$,

$$(2.2) \quad f(\boldsymbol{x}) = \frac{1}{(2\pi)^{d/2}} \sum_{n=1}^{\infty} \int_{\Gamma^*} u_n(\boldsymbol{\xi}, \boldsymbol{x}) e^{i\boldsymbol{\xi} \cdot \boldsymbol{x}} (\mathcal{B}f)_n(\boldsymbol{\xi}) \, d\boldsymbol{\xi},$$

where the Bloch transform $\mathcal{B} : L^2(\mathbb{R}^d) \rightarrow L^2(\Gamma^*)^{\mathbb{N}}$ is given by

$$(2.3) \quad (\mathcal{B}f)_n(\boldsymbol{\xi}) = \frac{1}{(2\pi)^{d/2}} \int_{\mathbb{R}^d} \bar{u}_n(\boldsymbol{\xi}, \mathbf{y}) e^{-i\boldsymbol{\xi} \cdot \mathbf{y}} f(\mathbf{y}) \, d\mathbf{y}.$$

As an analog to the Parseval's identity, it holds

$$(2.4) \quad \int_{\mathbb{R}^d} |f(\mathbf{x})|^2 \, d\mathbf{x} = \sum_{n=1}^{\infty} \int_{\Gamma^*} |(\mathcal{B}f)_n(\boldsymbol{\xi})|^2 \, d\boldsymbol{\xi}.$$

We denote Ω the phase space corresponding to one band

$$(2.5) \quad \Omega := \mathbb{R}^d \times \Gamma^* = \{(\mathbf{x}, \boldsymbol{\xi}) \mid \mathbf{x} \in \mathbb{R}^d, \boldsymbol{\xi} \in \Gamma^*\}.$$

Let us define the Berry phase, which will be used later, as

$$(2.6) \quad \mathcal{A}_n(\boldsymbol{\xi}) = \langle u_n(\boldsymbol{\xi}, \cdot) \mid i\nabla_{\boldsymbol{\xi}} u_n(\boldsymbol{\xi}, \cdot) \rangle_{L^2(\Gamma)}.$$

Here we have used the Dirac bra-ket notation $\langle \cdot \mid \cdot \rangle$ in quantum mechanics, i.e.,

$$\langle f \mid g \rangle_{L^2(\Omega)} = \int_{\Omega} \bar{f} g \, d\mathbf{y}, \quad \text{and} \quad \langle f \mid g \rangle = \int_{\mathbb{R}^d} \bar{f} g \, d\mathbf{y},$$

where \bar{f} is the complex conjugate of f . Note that the eigenvalue equation (1.3) and its normalization only define $u_n(\boldsymbol{\xi}, \cdot)$ up to a unit complex number, in particular, for any function ϕ periodic in Γ^*

$$(2.7) \quad \tilde{u}_n(\boldsymbol{\xi}, \mathbf{x}) = e^{i\phi(\boldsymbol{\xi})} u_n(\boldsymbol{\xi}, \mathbf{x})$$

also provides a set of Bloch waves. This is known as the gauge freedom for Bloch waves. It is known that (see *e.g.*, [22]) we can choose ϕ such that $\tilde{u}_n(\boldsymbol{\xi}, \mathbf{x})$ is smooth in $\boldsymbol{\xi}$, and then the definition (2.6) makes sense. However, different gauge choice might give different values of $\mathcal{A}_n(\boldsymbol{\xi})$, and it is also difficult in numerical diagonalization of the Bloch waves to make sure that the phase dependence is smooth. We will come back to this delicacy in the development of numerical algorithms. Note that from the normalization condition (1.2), $\mathcal{A}_n(\boldsymbol{\xi})$ is always a real number.

2.2. Formulation. We denote $G_{\mathbf{q}, \mathbf{p}}^\varepsilon$ the semiclassical Gaussian function localized in the phase space at (\mathbf{q}, \mathbf{p}) :

$$(2.8) \quad G_{\mathbf{q}, \mathbf{p}}^\varepsilon(\mathbf{x}) = \exp(-|\mathbf{x} - \mathbf{q}|^2/(2\varepsilon) + i\mathbf{p} \cdot (\mathbf{x} - \mathbf{q})/\varepsilon).$$

The frozen Gaussian approximation (FGA) solution to (1.1) with the initial condition ψ_0 is approximated by [3],

$$(2.9) \quad \psi_{\text{FGA}}^\varepsilon(t, \mathbf{x}) = \frac{1}{(2\pi\varepsilon)^{3d/2}} \sum_{n=1}^{\infty} \int_{\Omega} a_n(t, \mathbf{q}, \mathbf{p}) u_n(\mathbf{P}_n, \mathbf{x}/\varepsilon) G_{\mathbf{Q}_n, \mathbf{P}_n}^\varepsilon(\mathbf{x}) e^{iS_n(t, \mathbf{q}, \mathbf{p})/\varepsilon} \\ \times \langle G_{\mathbf{q}, \mathbf{p}}^\varepsilon u_n(\mathbf{p}, \cdot/\varepsilon) \mid \psi_0 \rangle \, d\mathbf{q} \, d\mathbf{p}.$$

The right hand side of (2.9) sums over all the Bloch bands. For each n , $(\mathbf{Q}_n(t, \mathbf{q}, \mathbf{p}), \mathbf{P}_n(t, \mathbf{q}, \mathbf{p}))$ solves the equation of motion given by the classical Hamiltonian $h_n(\mathbf{q}, \mathbf{p}) = E_n(\mathbf{p}) + U(\mathbf{q})$:

$$(2.10) \quad \begin{cases} \frac{d\mathbf{Q}_n}{dt} = \nabla E_n(\mathbf{P}_n), \\ \frac{d\mathbf{P}_n}{dt} = -\nabla U(\mathbf{Q}_n), \end{cases}$$

with the initial conditions $\mathbf{Q}_n(0, \mathbf{q}, \mathbf{p}) = \mathbf{q}$ and $\mathbf{P}_n(0, \mathbf{q}, \mathbf{p}) = \mathbf{p}$. For simplicity, we shall omit the subscripts of gradient whenever it does not cause any confusion.

In (2.9), $S_n(t, \mathbf{q}, \mathbf{p})$ is the action associated with the Hamiltonian dynamics (2.10), given by the evolution equation

$$(2.11) \quad \frac{dS_n}{dt} = \mathbf{P}_n \cdot \nabla_{\mathbf{P}} h_n(\mathbf{Q}_n, \mathbf{P}_n) - h_n(\mathbf{Q}_n, \mathbf{P}_n),$$

with the initial condition $S_n(0, \mathbf{q}, \mathbf{p}) = 0$. The function $a_n(t, \mathbf{q}, \mathbf{p})$ gives the amplitude of the Gaussian function at time t . With the short hand notations

$$(2.12) \quad \partial_{\mathbf{z}} = \partial_{\mathbf{q}} - i\partial_{\mathbf{p}} \quad Z_n = \partial_{\mathbf{z}} (\mathbf{Q}_n + i\mathbf{P}_n),$$

the evolution equation for a_n is given by

$$(2.13) \quad \frac{da_n}{dt} = -ia_n \mathcal{A}_n(\mathbf{P}_n) \cdot \nabla U(\mathbf{Q}_n) + \frac{1}{2} a_n \text{tr}(\partial_{\mathbf{z}} \mathbf{P}_n \nabla^2 E_n(\mathbf{P}_n) Z_n^{-1}) - \frac{i}{2} a_n \text{tr}(\partial_{\mathbf{z}} \mathbf{Q}_n \nabla^2 U(\mathbf{Q}_n) Z_n^{-1})$$

with initial condition $a_n(0, \mathbf{q}, \mathbf{p}) = 2^{d/2}$ for each (\mathbf{q}, \mathbf{p}) . Recall that $\mathcal{A}_n(\boldsymbol{\xi})$ is the Berry phase of the n -th Bloch band given in (2.6).

2.3. Gauge-Invariant Integrator. The gauge freedom of the eigenfunction $u_n(\boldsymbol{\xi}, \mathbf{x})$ of (1.4) causes problems for numerical computation. In particular, different choice of gauge may lead to different numerical results for the Berry phase term $\mathcal{A}_n(\boldsymbol{\xi}) = \langle u_n(\boldsymbol{\xi}, \mathbf{x}) | i\nabla_{\boldsymbol{\xi}} u_n(\boldsymbol{\xi}, \mathbf{x}) \rangle$, and hence different $\psi_{\text{FGA}}^\varepsilon$ which is artificial. It is desirable hence to design an algorithm that is manifestly independent of the gauge. The key is to avoid direct computation of the the Berry phase and so to avoid the the computation of the momentum-gradient of u_n .

First, we separate the dependence of a_n on \mathcal{A}_n in the evolution equation (2.13). For this, we define S_n^A the phase contribution due to the Berry phase term

$$(2.14) \quad S_n^A(t, \mathbf{q}, \mathbf{p}) = \int_0^t \mathcal{A}_n(\mathbf{P}_n) \cdot \nabla U(\mathbf{Q}_n) ds.$$

Let

$$b_n(t, \mathbf{q}, \mathbf{p}) = a_n(t, \mathbf{q}, \mathbf{p}) \exp(iS_n^A(t, \mathbf{q}, \mathbf{p})),$$

then it solves

$$(2.15) \quad \frac{db_n}{dt} = \frac{1}{2} b_n \text{tr}(\partial_{\mathbf{z}} \mathbf{P}_n \nabla^2 E_n(\mathbf{P}_n) Z_n^{-1}) - \frac{i}{2} b_n \text{tr}(\partial_{\mathbf{z}} \mathbf{Q}_n \nabla^2 U(\mathbf{Q}_n) Z_n^{-1}),$$

with initial condition $b_n(0, \mathbf{q}, \mathbf{p}) = 2^{d/2}$. The evolution equation (2.15) for b_n is *manifestly gauge-invariant*, as all terms are independent of the gauge choice. Using the amplitude function b_n , the frozen Gaussian approximation can be rewritten as

$$(2.16) \quad \psi_{\text{FGA}}^\varepsilon(t, \mathbf{x}) = \frac{1}{(2\pi\varepsilon)^{3d/2}} \sum_{n=1}^{\infty} \int_{\Gamma^*} \int_{\mathbb{R}^d} b_n(t, \mathbf{q}, \mathbf{p}) u_n(\mathbf{P}_n, \mathbf{x}/\varepsilon) G_{\mathbf{Q}_n, \mathbf{P}_n}^\varepsilon(\mathbf{x}) e^{iS_n(t, \mathbf{q}, \mathbf{p})/\varepsilon - iS_n^A(t, \mathbf{q}, \mathbf{p})} \\ \times \langle G_{\mathbf{q}, \mathbf{p}}^\varepsilon u_n(\mathbf{p}, \cdot/\varepsilon) | \psi_0 \rangle d\mathbf{q} d\mathbf{p}.$$

The gauge-dependent term in (2.16) thus reads

$$(2.17) \quad u_n(\mathbf{P}_n, \mathbf{x}/\varepsilon) e^{-iS_n^A(t, \mathbf{q}, \mathbf{p})} \bar{u}_n(\mathbf{p}, \mathbf{y}/\varepsilon).$$

Our goal is hence to design a gauge-invariant time integrator for (2.14) such that the term (2.17) becomes independent of the gauge. Observe that, by the Hamiltonian flow (2.10),

$$(2.18) \quad S_n^A(t, \mathbf{q}, \mathbf{p}) = - \int_0^t \mathcal{A}(\mathbf{P}_n) \cdot d\mathbf{P}_n(s).$$

Let $0 = t_0 < t_1 < \dots < t_K = t$ be a time discretization, we have

$$(2.19) \quad \exp(-iS_n^A) = \exp\left(i \int_0^t \mathcal{A}(\mathbf{P}_n) \cdot d\mathbf{P}_n(s)\right) = \prod_{k=1}^K \exp\left(i \int_{t_{k-1}}^{t_k} \mathcal{A}(\mathbf{P}_n) \cdot d\mathbf{P}_n(s)\right).$$

To proceed, let us first work in a gauge where $u_n(\boldsymbol{\xi}, \cdot)$ is smooth in $\boldsymbol{\xi} \in \Gamma^*$. Note that since our final formula is gauge-independent, the choice of the gauge here is only for the derivation. Using the Taylor approximation, we obtain

$$(2.20) \quad \begin{aligned} i \int_{t_{k-1}}^{t_k} \mathcal{A}(\mathbf{P}_n) \cdot d\mathbf{P}_n(s) &= -i \Im \{ \langle u_n(\mathbf{P}_n(t_{k-1}), \cdot) | \nabla u_n(\mathbf{P}_n(t_{k-1}), \cdot) \rangle \cdot \Delta \mathbf{P}_{k,n} \} + \mathcal{O}(\Delta \mathbf{P}_{k,n})^2 \\ &= i \Im \{ 1 - \langle u_n(\mathbf{P}_n(t_{k-1}), \cdot) | u_n(\mathbf{P}_n(t_k), \cdot) \rangle \} + \mathcal{O}(\Delta \mathbf{P}_{k,n})^2 \\ &= i \Im \{ \ln \langle u_n(\mathbf{P}_n(t_k), \cdot) | u_n(\mathbf{P}_n(t_{k-1}), \cdot) \rangle \} + \mathcal{O}(\Delta \mathbf{P}_{k,n})^2, \end{aligned}$$

where $\Delta \mathbf{P}_{k,n} = \mathbf{P}_n(t_k) - \mathbf{P}_n(t_{k-1})$. The first approximation was obtained by using a left Riemann sum. The next approximation is the forward difference approximation for the derivative. The last approximation is the Taylor series for $\ln z$ around $z = 1$. Therefore, taking exponential, we get

$$(2.21) \quad \exp\left(i \int_{t_{k-1}}^{t_k} \mathcal{A}(\mathbf{P}_n) \cdot d\mathbf{P}_n(s)\right) = \frac{\langle u_n(\mathbf{P}_n(t_k), \cdot) | u_n(\mathbf{P}_n(t_{k-1}), \cdot) \rangle}{|\langle u_n(\mathbf{P}_n(t_k), \cdot) | u_n(\mathbf{P}_n(t_{k-1}), \cdot) \rangle|} + \mathcal{O}(\Delta \mathbf{P}_{k,n})^2.$$

Substituting the last equation in the right hand side of (2.19) gives an approximation to $\exp(-iS_n^A)$ with an error $\mathcal{O}(\Delta \mathbf{P}_n)$ with $\Delta \mathbf{P}_n = \max_k |\Delta \mathbf{P}_{k,n}|$. This then gives the approximation to (2.17) as

$$(2.22) \quad \begin{aligned} u_n(\mathbf{P}_n, \mathbf{x}/\varepsilon) e^{-iS_n^A(t, \mathbf{q}, \mathbf{p})} \bar{u}_n(\mathbf{p}, \mathbf{y}/\varepsilon) &= F_n(t, \mathbf{q}, \mathbf{p}, \mathbf{x}, \mathbf{y}) + \mathcal{O}(\Delta \mathbf{P}_n) \\ &:= |u_n(\mathbf{P}_n(t_K), \mathbf{x}/\varepsilon)\rangle \prod_{k=1}^K \frac{\langle u_n(\mathbf{P}_n(t_k), \cdot) | u_n(\mathbf{P}_n(t_{k-1}), \cdot) \rangle}{|\langle u_n(\mathbf{P}_n(t_k), \cdot) | u_n(\mathbf{P}_n(t_{k-1}), \cdot) \rangle|} \langle u_n(\mathbf{P}_n(t_0), \mathbf{y}/\varepsilon) | + \mathcal{O}(\Delta \mathbf{P}_n). \end{aligned}$$

The right hand side of (2.22) is manifestly gauge-invariant, as the phase term in $|u_n(\mathbf{P}_n(t_k), \cdot)\rangle$ will cancel with that of $\langle u_n(\mathbf{P}_n(t_k), \cdot)|$, for $k = 0, \dots, K$.

Therefore, in summary, we arrive at a gauge-invariant reformulation of $\psi_{\text{FGA}}^\varepsilon$ as

$$(2.23) \quad \begin{aligned} \psi_{\text{FGA}}^\varepsilon(t, \mathbf{x}) &\approx \frac{1}{(2\pi\varepsilon)^{3d/2}} \sum_{n=1}^{\infty} \int_{\Gamma^*} \int_{\mathbb{R}^d} b_n(t, \mathbf{q}, \mathbf{p}) F_n(t, \mathbf{q}, \mathbf{p}, \mathbf{x}, \mathbf{y}) G_{\mathbf{Q}_n, \mathbf{P}_n}^\varepsilon(\mathbf{x}) \\ &\quad \times e^{iS_n(t, \mathbf{q}, \mathbf{p})/\varepsilon} \langle G_{\mathbf{q}, \mathbf{p}}^\varepsilon | \psi_0 \rangle d\mathbf{q} d\mathbf{p}, \end{aligned}$$

where F_n is given by (2.22), and the evolution of $(\mathbf{Q}_n, \mathbf{P}_n)$ follows the Hamiltonian dynamics

$$(2.24) \quad \begin{cases} \frac{d\mathbf{Q}_n}{dt} = \nabla E_n(\mathbf{P}_n), \\ \frac{d\mathbf{P}_n}{dt} = -\nabla U(\mathbf{Q}_n), \end{cases}$$

with initial condition $\mathbf{Q}_n(0, \mathbf{q}, \mathbf{p}) = \mathbf{q}$ and $\mathbf{P}_n(0, \mathbf{q}, \mathbf{p}) = \mathbf{p}$.

The action S_n solves

$$(2.25) \quad \frac{dS_n}{dt} = \mathbf{P}_n \cdot \nabla_{\mathbf{P}} h_n(\mathbf{Q}_n, \mathbf{P}_n) - h_n(\mathbf{Q}_n, \mathbf{P}_n),$$

with initial condition $S_n(0, \mathbf{q}, \mathbf{p}) = 0$, and the amplitude b_n follows the evolution

$$(2.26) \quad \frac{db_n}{dt} = \frac{1}{2} b_n \text{tr} (\partial_z \mathbf{P}_n \nabla^2 E_n(\mathbf{P}_n) Z_n^{-1}) - \frac{i}{2} b_n \text{tr} (\partial_z \mathbf{Q}_n \nabla^2 U_n(\mathbf{Q}_n) Z_n^{-1}),$$

with initial condition $b_n(0, \mathbf{q}, \mathbf{p}) = 2^{d/2}$.

2.4. Analytical Results. To make the presentation self-contained, we briefly recall here the analytical results proved in [3] for the frozen Gaussian approximation to (1.1). The proofs of these results and more details can be found in [3].

First we recall that the FGA ansatz recover the initial condition at time $t = 0$, $\psi_{\text{FGA}}^\varepsilon(0, \mathbf{x}) = \psi_0(\mathbf{x})$. This follows from the Bloch decomposition (2.2).

Let us recall a few notions from [3] to state the convergence results for the frozen Gaussian approximation. We define the windowed Bloch transform $(\mathcal{W}f)_n(\mathbf{q}, \mathbf{p}) : L^2(\mathbb{R}^d) \rightarrow L^2(\Omega)^\mathbb{N}$ as

$$(2.27) \quad (\mathcal{W}f)_n(\mathbf{q}, \mathbf{p}) = \frac{2^{d/4}}{(2\pi)^{3d/4}} \langle u_n(\mathbf{p}, \cdot) G_{\mathbf{q}, \mathbf{p}} | f \rangle = \frac{2^{d/4}}{(2\pi)^{3d/4}} \int_{\mathbb{R}^d} \bar{u}_n(\mathbf{p}, \mathbf{x}) \bar{G}_{\mathbf{q}, \mathbf{p}}(\mathbf{x}) f(\mathbf{x}) d\mathbf{x}$$

where

$$(2.28) \quad G_{\mathbf{q}, \mathbf{p}}(\mathbf{x}) := \exp\left(-\frac{|\mathbf{x} - \mathbf{q}|^2}{2} + i\mathbf{p} \cdot (\mathbf{x} - \mathbf{q})\right).$$

The adjoint operator $\mathcal{W}^* : L^2(\Omega)^\mathbb{N} \rightarrow L^2(\mathbb{R}^d)$ is then

$$(2.29) \quad (\mathcal{W}^*g)(\mathbf{x}) = \frac{2^{d/4}}{(2\pi)^{3d/4}} \sum_{n=1}^{\infty} \iint_{\Omega} u_n(\mathbf{p}, \mathbf{x}) G_{\mathbf{q}, \mathbf{p}}(\mathbf{x}) g_n(\mathbf{q}, \mathbf{p}) d\mathbf{q} d\mathbf{p}.$$

The windowed Bloch transform and its adjoint have the following important property.

Proposition ([3, Proposition 2.2]). *The windowed Bloch transform and its adjoint satisfies*

$$(2.30) \quad \mathcal{W}^* \mathcal{W} = \text{Id}_{L^2(\mathbb{R}^d)}.$$

Remark. Similar to the windowed Fourier transform, the representation given by the windowed Bloch transform is redundant, so that $\mathcal{W}\mathcal{W}^* \neq \text{Id}_{L^2(\Omega)^\mathbb{N}}$. The normalization constant in the definition of \mathcal{W} is also due to this redundancy.

The previous proposition motivates us to consider the contribution of each band to the reconstruction formulae (2.30). This gives to the operator $\Pi_n^{\mathcal{W}} : L^2(\mathbb{R}^d) \rightarrow L^2(\mathbb{R}^d)$ for each $n \in \mathbb{N}$

$$(2.31) \quad (\Pi_n^{\mathcal{W}} f)(\mathbf{x}) = \frac{2^{d/4}}{(2\pi)^{3d/4}} \iint_{\Omega} u_n(\mathbf{p}, \mathbf{x}) G_{\mathbf{q}, \mathbf{p}}(\mathbf{x}) (\mathcal{W}f)_n(\mathbf{q}, \mathbf{p}) d\mathbf{q} d\mathbf{p}.$$

It follows from (2.30) that $\sum_n \Pi_n^{\mathcal{W}} = \text{Id}_{L^2(\mathbb{R}^d)}$.

Correspondingly, the semiclassical windowed Bloch transform $\mathcal{W}^\varepsilon : L^2(\mathbb{R}^d) \rightarrow L^2(\Omega)^\mathbb{N}$ is defined as

$$(2.32) \quad (\mathcal{W}^\varepsilon f)_n(\mathbf{q}, \mathbf{p}) = \frac{2^{d/4}}{(2\pi\varepsilon)^{3d/4}} \langle u_n(\mathbf{p}, \cdot/\varepsilon) G_{\mathbf{q}, \mathbf{p}}^\varepsilon | f \rangle = \frac{2^{d/4}}{(2\pi\varepsilon)^{3d/4}} \int_{\mathbb{R}^d} \bar{u}_n(\mathbf{p}, \mathbf{x}/\varepsilon) \bar{G}_{\mathbf{q}, \mathbf{p}}^\varepsilon(\mathbf{x}) f(\mathbf{x}) d\mathbf{x}.$$

Similarly we also have the operator $\Pi_n^{\mathcal{W}, \varepsilon} : L^2(\mathbb{R}^d) \rightarrow L^2(\mathbb{R}^d)$ for each $n \in \mathbb{N}$ with semiclassical scaling

$$(2.33) \quad (\Pi_n^{\mathcal{W}, \varepsilon} f)(\mathbf{y}) = \frac{2^{d/4}}{(2\pi\varepsilon)^{3d/4}} \iint_{\Omega} u_n(\boldsymbol{\xi}, \mathbf{y}/\varepsilon) G_{\mathbf{x}, \boldsymbol{\xi}}^\varepsilon(\mathbf{y}) (\mathcal{W}^\varepsilon f)_n(\mathbf{x}, \boldsymbol{\xi}) d\mathbf{x} d\boldsymbol{\xi}.$$

It follows from (2.30) and a change of variable that $\sum_n \Pi_n^{\mathcal{W}, \varepsilon} = \text{Id}_{L^2(\mathbb{R}^d)}$.

For the long time existence of the Hamiltonian flow (2.10), we will assume that the external potential $U(\mathbf{x})$ is subquadratic, such that $\|\partial_{\mathbf{x}}^\alpha U(\mathbf{x})\|_{L^\infty}$ is finite for all multi-index $|\alpha| \geq 2$. As a result, since the domain of $\boldsymbol{\xi}$ is bounded, the Hamiltonian h_n is also subquadratic. $\psi_{\text{FGA}}^\varepsilon$ provides an approximate solution to equation (1.1) to first order accuracy as stated in the two theorems below, rephrased from our previous work [3].

Theorem ([3, Theorem 3.1]). *Assume that the n -th Bloch band $E_n(\boldsymbol{\xi})$ does not intersect any other Bloch bands for all $\boldsymbol{\xi} \in \Gamma^*$; and moreover, the Hamiltonian $h_n(\mathbf{x}, \boldsymbol{\xi})$ is subquadratic. Let $\mathcal{U}_t^\varepsilon$ be the propagator of the time-dependent Schrödinger equation (1.1). Then for any given T , $0 \leq t \leq T$ and sufficiently small, $\varepsilon \leq \varepsilon_0$,*

$$(2.34) \quad \sup_{0 \leq t \leq T} \left\| \mathcal{U}_t^\varepsilon (\Pi_n^{\mathcal{W}, \varepsilon} \psi_0) - \frac{1}{(2\pi\varepsilon)^{3d/2}} \int_{\Omega} b_n(t, \mathbf{q}, \mathbf{p}) u_n(\mathbf{P}_n, \mathbf{x}/\varepsilon) G_{\mathbf{Q}_n, \mathbf{P}_n}^\varepsilon(\mathbf{x}) \times \right. \\ \left. \times e^{iS_n(t, \mathbf{q}, \mathbf{p})/\varepsilon - iS_n^A(t, \mathbf{q}, \mathbf{p})} \langle G_{\mathbf{q}, \mathbf{p}}^\varepsilon u_n(\mathbf{p}, \cdot/\varepsilon) | \psi_0 \rangle d\mathbf{q} d\mathbf{p} \right\|_{L^2} \leq C_{T, n} \varepsilon \|\psi_0^\varepsilon\|_{L^2}.$$

Theorem ([3, Theorem 3.2]). *Assume that the first N Bloch bands $E_n(\boldsymbol{\xi})$, $n = 1, \dots, N$ do not intersect and are separated from the other bands for all $\boldsymbol{\xi} \in \Gamma^*$; and assume that the Hamiltonian $h_n(\mathbf{x}, \boldsymbol{\xi})$ is subquadratic. Let $\mathcal{U}_t^\varepsilon$ be the propagator of the time-dependent Schrödinger equation (1.1). Then for any given T , $0 \leq t \leq T$ and sufficiently small ε , we have*

$$(2.35) \quad \sup_{0 \leq t \leq T} \left\| \mathcal{U}_t^\varepsilon \psi_0 - \frac{1}{(2\pi\varepsilon)^{3d/2}} \sum_{n=1}^N \int_{\Omega} b_n(t, \mathbf{q}, \mathbf{p}) u_n(\mathbf{P}_n, \mathbf{x}/\varepsilon) G_{\mathbf{Q}_n, \mathbf{P}_n}^\varepsilon(\mathbf{x}) e^{iS_n(t, \mathbf{q}, \mathbf{p})/\varepsilon - iS_n^A(t, \mathbf{q}, \mathbf{p})} \times \right. \\ \left. \times \langle G_{\mathbf{q}, \mathbf{p}}^\varepsilon u_n(\mathbf{p}, \cdot/\varepsilon) | \psi_0 \rangle d\mathbf{q} d\mathbf{p} \right\|_{L^2} \leq C_{T, N} \varepsilon \|\psi_0^\varepsilon\|_{L^2} + \|\psi_0^\varepsilon - \sum_{n=1}^N \Pi_n^{\mathcal{W}, \varepsilon} \psi_0^\varepsilon\|_{L^2}.$$

These approximation results show the first order asymptotic accuracy of FGA, which will be numerically validated in Section 4.

3. NUMERICAL IMPLEMENTATION

We will now describe the numerical implementation of the gauge-invariant frozen Gaussian approximation (GIFGA) method. We will restrict ourselves to one spatial dimension in this paper. For one thing, the computation of true solutions to (1.1) with high accuracy is extremely time-consuming in high dimensions, and thus it is difficult for us to confirm numerically the asymptotic convergence order with the pollution of non-negligible numerical errors. For another thing, band-crossing is quite common in high dimensional cases (e.g., in honeycomb lattice), which requires more techniques than the scope of this paper, and we will leave the numerical study of high dimensional examples as future work. The calculation of the Bloch eigenvalues and eigenfunctions is discussed in Section 3.1. In Section 3.2 We describe the numerical algorithms of GIFGA based on the Bloch bands. We will also discuss the mesh sizes required for accurate computation.

3.1. Numerical computation of Bloch bands. We show how to compute numerically the eigenvalues and eigenfunctions of (1.3) in $d = 1$. Define the Fourier transform of $u_n(\boldsymbol{\xi}, x)$ as

$$(3.1) \quad \widehat{u}_n(\boldsymbol{\xi}, \eta) = \frac{1}{2\pi} \int_{\Gamma} u_n(\boldsymbol{\xi}, x) e^{-ix\eta} dx.$$

Taking the Fourier transform of (1.3) one obtains

$$(3.2) \quad \frac{(\eta + \boldsymbol{\xi})^2}{2} \widehat{u}_n(\boldsymbol{\xi}, \eta) + \widehat{V}_\Gamma(\eta) * \widehat{u}_n(\boldsymbol{\xi}, \eta) = E_n(\boldsymbol{\xi}) \widehat{u}_n(\boldsymbol{\xi}, \eta),$$

where “*” stands for the operation of convolution.

Truncating the Fourier grid to $\{-\Lambda, \dots, \Lambda - 1\} \subset \mathbb{Z}$ gives

$$(3.3) \quad H_\xi(\Lambda) \begin{pmatrix} \widehat{u}_n(\xi, -\Lambda) \\ \widehat{u}_n(\xi, 1 - \Lambda) \\ \vdots \\ \widehat{u}_n(\xi, \Lambda - 1) \end{pmatrix} = E_n(\xi) \begin{pmatrix} \widehat{u}_n(\xi, -\Lambda) \\ \widehat{u}_n(\xi, 1 - \Lambda) \\ \vdots \\ \widehat{u}_n(\xi, \Lambda - 1) \end{pmatrix}$$

where $H_\xi(\Lambda)$ is the $2\Lambda \times 2\Lambda$ matrix given by

$$(3.4) \quad H_\xi(\Lambda) = \begin{pmatrix} \frac{(-\Lambda + \xi)^2}{2} + \widehat{V}_\Gamma(0) & \widehat{V}_\Gamma(-1) & \cdots & \widehat{V}_\Gamma(1 - 2\Lambda) \\ \widehat{V}_\Gamma(1) & \frac{(-\Lambda + 1 + \xi)^2}{2} + \widehat{V}_\Gamma(0) & \cdots & \widehat{V}_\Gamma(2 - 2\Lambda) \\ \cdots & \cdots & \ddots & \cdots \\ \widehat{V}_\Gamma(2\Lambda - 1) & \widehat{V}_\Gamma(2\Lambda - 2) & \cdots & \frac{(\Lambda - 1 + \xi)^2}{2} + \widehat{V}_\Gamma(0) \end{pmatrix}.$$

After diagonalizing the matrix, the eigenfunction in the physical domain is then obtained via inverse Fourier transform

$$(3.5) \quad u_n(\xi, x) \approx \sum_{y=-\Lambda}^{\Lambda-1} \widehat{u}_n(\xi, \eta) e^{i\eta x}.$$

Example 3.1. *In this example, we compute Bloch eigenvalues and eigenfunctions with potential $V_\Gamma(x) = \exp(-25x^2)$. The extension of $V_\Gamma(x)$ periodically with respect to Γ is not analytic on the boundary of Γ . However, this lack of smoothness presents a negligible problem numerically as $V_\Gamma(x)$ decays rapidly. Figure 1 shows the energy eigenvalues $E_n(\xi)$ for $\xi \in [0, 1)$. The plot shows the first 8 bands where the bottom curve corresponds to $n = 1$ (lowest band) and the top curve represents $n = 8$ (highest band). Figure 2 shows the modules of the corresponding Bloch eigenfunctions for the first 4 bands. Notice that while these surfaces are continuous and periodic, the next two figures (3 and 4) of the real and imaginary parts of the Bloch eigenfunctions are not. This is due to the arbitrary gauge freedom in the diagonalization.*

Remark. 1. In the numerical computation of $E(\xi)$, the corresponding eigenfunctions and their derivatives near the points $\xi = 0$ and $\xi = 0.5$ (and $\xi = 1$ by periodicity) is tricky, since the Bloch bands are close to each other near these points (see Figure 1). For this reason, our grid for the ξ variable will not contain these points. In other words, we shift the grids in the first Brillouin zone to avoid these high symmetry points.

2. One can apply the same technique to derive an algorithm for computing Bloch eigenvalues and eigenfunctions in higher dimensions. The main issue with this algorithm is that the numerical cost increases drastically for $d > 1$. In the case where the periodic potential has the form $V_\Gamma(\mathbf{x}) = \sum_{j=1}^d V_j(x_j)$ with $V_j(x_j + 2\pi) = V_j(x_j)$, computation of Bloch bands can be treated for each coordinate x_j separately. For some common potentials, data for the energy eigenvalues has already been produced (see remark 2.1 in [8]).

3.2. Algorithms for gauge invariant frozen Gaussian approximation. We assume that the initial data $\psi_0(x)$ has compact support or that it decays sufficiently fast as $|x| \rightarrow \infty$, and hence, we only need to use a finite number of mesh points in physical space.

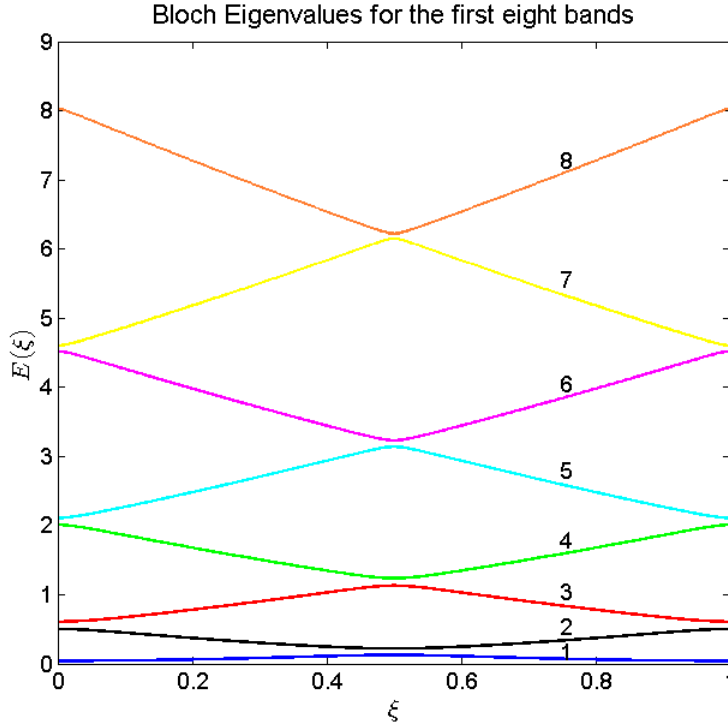


FIGURE 1. Energy eigenvalues for the one-dimensional lattice potential $V(x) = \exp(-25x^2)$

For a mesh size δx and starting point $x^0 \in \mathbb{R}$, the grid is specified as

$$(3.6) \quad x^m = x^0 + (m - 1)\delta x,$$

for $m = 1, \dots, N_x$, where N_x is the number of the spatial grid in one dimension.

We present the algorithm in five steps below.

Step 1. Compute the Bloch eigenvalues $E_n(\xi)$ and eigenfunctions $u_n(\xi, x)$ of (1.3), according to the algorithm described in Section 3.1.

Remark. For our one dimensional examples in Section 4, we choose a mesh for (ξ, x) such that $\delta\xi = (1 - 2\rho)/199$ with $\xi^0 = -1/2 + \rho$ and $N_\xi = 200$; and $\delta x = 2\pi/804$ with $x^0 = -\pi$ and $N_x = 805$ for some $0 < \rho \ll 1$. ρ was included to avoid putting mesh points at high symmetry points in the first Brillouin zone. This number of grid points is enough to ensure that the eigenvalues and eigenfunctions are computed with sufficient accuracy for our numerical tests.

Step 2. Compute $(Q_n(t, q, p), P_n(t, q, p), S_n(t, q, p), b_n(t, q, p))$ in (2.24), (2.25), and (2.26).

To integrate the ODEs for (Q_n, P_n, S_n, b_n) , we use a symplectic fourth order Runge-Kutta method. Coefficients for the Butcher tableau can be found in [23]. We will choose a mesh for $(q, p) \in \Omega$ and (Q_n, P_n) takes initial value at the grid points. That is,

$$(3.7) \quad Q_n(0, q, p) = q^I = q^0 + I\delta q$$

$$(3.8) \quad P_n(0, q, p) = p^J = p^0 + J\delta p$$

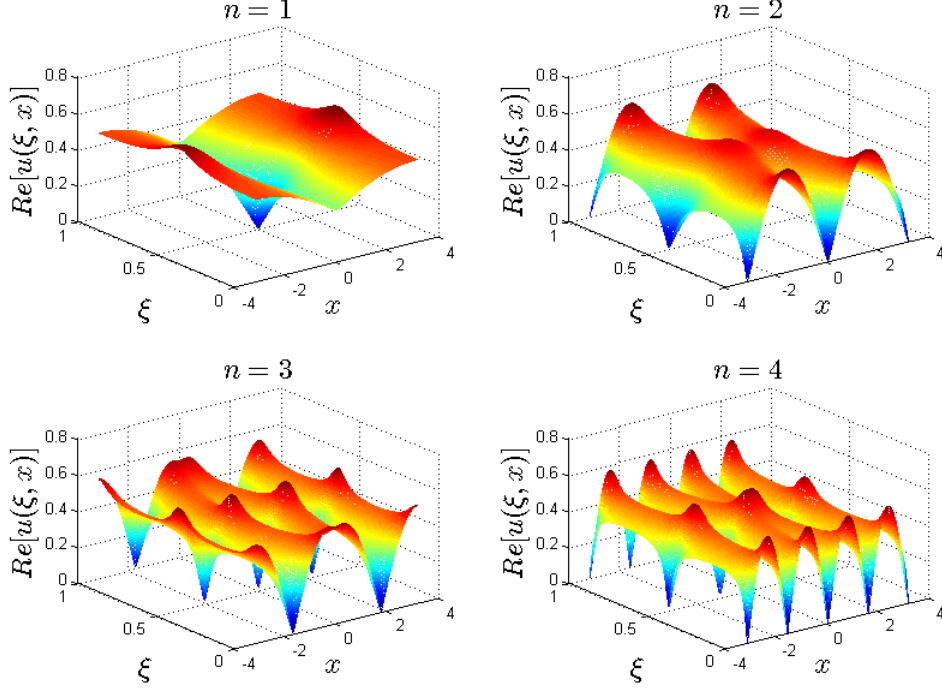


FIGURE 2. Module of eigenfunctions for the one-dimensional lattice potential $V(x) = \exp(-25x^2)$. We display absolute value of the first 4 lowest energy eigenfunctions.

where $I \in 1, \dots, N_I$ and $J \in 1, \dots, N_J$. Notice that to represent the initial condition $\psi_{\text{FGA}}^\varepsilon(0, x)$ one only needs the mesh points q^I near x . To be more precise, as the standard deviation of the semiclassical Gaussians in (2.8) is $\sqrt{\varepsilon}$ so one only needs the mesh points q^I contributing significantly to $\psi_{\text{FGA}}^\varepsilon(0, x)$ satisfy $|x - q^I| \leq \mathcal{O}(\sqrt{\varepsilon})$. This implies that one can put a finite number of mesh points for q -coordinate and not on all of \mathbb{R} . The mesh size for q^I and p^J is chosen to be $\mathcal{O}(\sqrt{\varepsilon})$, which resolves the oscillation of the initial condition.

Step 3. Compute the windowed Bloch transformation of the initial condition $\langle u_n(p, \cdot/\varepsilon) G_{q,p}^\varepsilon | \psi_0 \rangle$. For the sake of convenience, denote this term by $w_n^\varepsilon(q, p)$. Let

$$(3.9) \quad y^K = y^0 + (K - 1)\delta y$$

be a discrete mesh of y where $K = 1, \dots, N_y$. Then,

$$(3.10) \quad w_n^\varepsilon(q^I, p^J) \approx \sum_{K=1}^{N_y} \bar{G}_{q^I, p^J}^\varepsilon(y^K) \bar{u}(p^J, y^K/\varepsilon) \psi_0(y^K) r_\theta(|y^K - q^I|) \delta y,$$

with r_θ a cut-off function such that $r_\theta = 1$ in the ball of radius $\theta > 0$ centered at the origin and $r_\theta = 0$ outside the ball.

The mesh y^K should approximately cover the support of the initial condition $\psi_0(y)$. As can be seen by the form of w_n^ε , the size of N_y will depend on ε . The mesh should be fine enough to accurately capture $\bar{u}_n(p, y/\varepsilon) \bar{G}_{q,p}^\varepsilon(y) \psi_0(y)$ for all bands n .

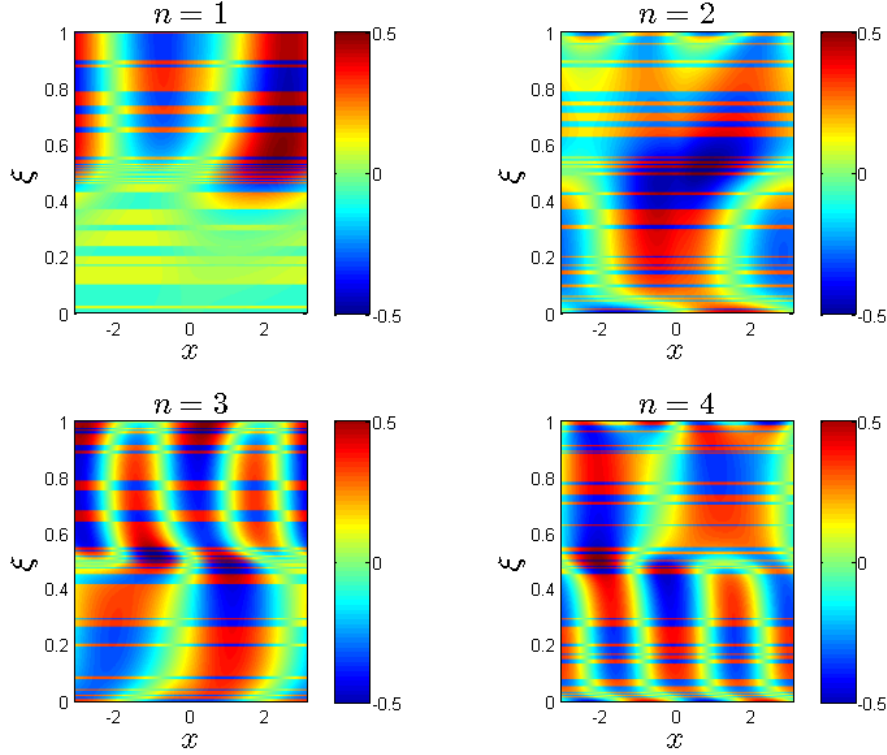


FIGURE 3. Real part of the eigenfunctions for the one-dimensional lattice potential $V(x) = \exp(-25x^2)$. We display the real parts for the first 4 lowest energy eigenfunctions. We use 100 data points for the ξ variable.

Remark. One can reduce the computation time of $w_n^\varepsilon(q^I, p^J)$ by incorporating the periodicity of $u_n(\xi, x)$ with respect to x . As can be seen by Figure 2, $u_n(\xi, x)$ tends to become more oscillatory as n increases. Thus, the mesh of y^K should be adapted so that it depends on n .

Step 4. Denote the product term in (2.22) by

$$(3.11) \quad \tilde{F}_n(t, q, p) := \prod_{k=1}^K \frac{\langle u(P_n(t_k), \cdot), u(P_n(t_{k-1}), \cdot) \rangle}{|\langle u(P_n(t_k), \cdot), u(P_n(t_{k-1}), \cdot) \rangle|},$$

and note that

$$F_n(t, q, p, x, y) = |u_n(P_n(t_K), x/\varepsilon) \tilde{F}_n(t, q, p) \langle u_n(P_n(t_0), y/\varepsilon) |.$$

At this point we now have the required data to compute \tilde{F}_n . Discretize \tilde{F}_n using the same mesh from the previous steps to obtain $\tilde{F}_n(t, q^I, p^J)$. Here, $t_0 = 0 \leq t_1 \leq t_2 \leq \dots \leq t_K = t$ is the temporal mesh used in Step 2, with

$$t_j = j\delta t, \quad \delta t = \frac{t}{K}, \quad \text{and } j = 1, \dots, K.$$

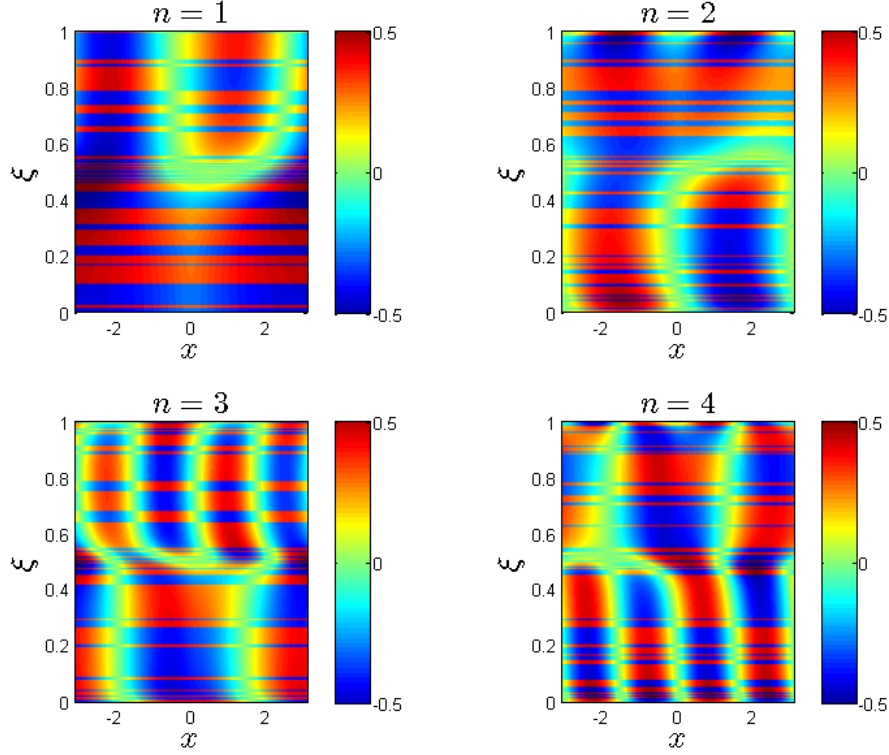


FIGURE 4. Imaginary part of the eigenfunctions for the one-dimensional lattice potential $V(x) = \exp(-25x^2)$. We display the imaginary parts for the first 4 lowest energy eigenfunctions. We use 100 data points for the ξ variable.

Step 5. Reconstruct the solution using (2.23)

$$(3.12) \quad \begin{aligned} \psi_{\text{FGA}}^\varepsilon(t, x^L) \approx & \sum_{n=1}^N \sum_I \sum_J \left(b_n(t, q^I, p^J) \bar{u}_n(P_n(t, q^I, p^J), x^L/\varepsilon) G_{Q_n, P_n}^\varepsilon(x^L) e^{S_n(t, q^I, p^J)/\varepsilon} \right. \\ & \left. \times \tilde{F}_n(t, q^I, p^J) \tilde{\psi}_n^\varepsilon(q^I, p^J) r_\theta(|x^L - Q_n^{I, J}|) \right) \delta q \delta p, \end{aligned}$$

where Q_n and P_n are evaluated at (t, q^I, p^J) , and r_θ is a cutoff function as described in Step 3 and N is the maximum number of Bloch bands used.

Accuracy. The theorems in Section 2.4 and (2.22) imply the above algorithm has a total accuracy $\mathcal{O}(\varepsilon + \delta t^4/\varepsilon + \max_n \Delta P_n) + \|\psi_0^\varepsilon - \sum_{n=1}^N \Pi_n^{\mathcal{W}, \varepsilon} \psi_0^\varepsilon\|_{L^2}$, where $\mathcal{O}(\delta t^4/\varepsilon)$ comes from the approximation to the phase functions in (2.23) and $\mathcal{O}(\max_n \Delta P_n) \approx \mathcal{O}(\delta t)$ is due to the approximation (2.22). $\|\psi_0^\varepsilon - \sum_{n=1}^N \Pi_n^{\mathcal{W}, \varepsilon} \psi_0^\varepsilon\|_{L^2}$ is the initial decomposition error, which in general decays with the number of bands as indicated in, e.g., Examples 4.1 and 4.2, and in [8].

$\varepsilon = 1/64$	Error $\ \psi_0 - \psi_{\text{FGA}}^\varepsilon\ _{L^2}$
$N = 1$	0.13260
$N = 2$	0.11328
$N = 4$	0.033126
$N = 8$	7.2587e-05
$\varepsilon = 1/128$	Error $\ \psi_0 - \psi_{\text{FGA}}^\varepsilon\ _{L^2}$
$N = 1$	0.15361
$N = 2$	0.096905
$N = 4$	0.031652
$N = 8$	7.0574e-05
$\varepsilon = 1/256$	Error $\ \psi_0 - \psi_{\text{FGA}}^\varepsilon\ _{L^2}$
$N = 1$	0.14165
$N = 2$	0.1063
$N = 4$	0.032405
$N = 8$	6.9192e-05
$\varepsilon = 1/512$	Error $\ \psi_0 - \psi_{\text{FGA}}^\varepsilon\ _{L^2}$
$N = 1$	0.15885
$N = 2$	0.09276
$N = 4$	0.031263
$N = 8$	6.8701e-05

TABLE 1. L^2 error of $\psi_0(x) - \psi_{\text{FGA}}^\varepsilon(0, x)$ for Example 4.1. We display various values of ε and sum over N Bloch bands in $\psi_{\text{FGA}}^\varepsilon$.

4. NUMERICAL EXAMPLES

In this section, we show the numerical performance of gauge invariant frozen Gaussian approximation (GIFGA) by several one dimensional examples, which also confirm the first order asymptotic convergency analyzed in [3].

4.1. Initial decomposition. In the first two examples, we test the initial decomposition of GIFGA described in Section 2. We compute $\psi_{\text{FGA}}^\varepsilon$ at $t = 0$ via equation (2.9). As we cannot numerically sum to infinity, we choose to use at most 8 bands in all of our examples. Expressed differently, the solution will be concentrated on the first 8 bands. Because of the need for $\mathcal{O}(\sqrt{\varepsilon})$ mesh size for both coordinates (q^I, p^J) of phase space, we choose approximately $2/\sqrt{\varepsilon}$ number of grid points for each unit interval.

Example 4.1. In this example, we check the initial decomposition by choosing $\psi_0 = A(x) \exp(iS(x)/\varepsilon)$ with $A(x) = \exp(-50x^2) \cos((x - 0.5)/\varepsilon)$ and $S(x) = 0.3(x - 0.5) + 0.1 \sin(x - 0.5)$, and the lattice potential $V_\Gamma = \cos(x)$. We record the data in Table 1.

Example 4.2. In this example, we check the initial decomposition by choosing $\psi_0 = A(x) \exp(iS(x)/\varepsilon)$ with $A(x) = \exp(-50x^2)$ and $S(x) = 0.3 + 0.1 \sin(x - 0.5)$, and the lattice potential to be $V_\Gamma = \exp(-25x^2)$. We record the data in Table 2.

$\varepsilon = 1/64$	Error $\ \psi_0 - \psi_{\text{FGA}}^\varepsilon\ _{L^2}$
$N = 1$	0.035736
$N = 2$	0.02463
$N = 4$	0.0075756
$N = 8$	0.0018796
$\varepsilon = 1/128$	Error $\ \psi_0 - \psi_{\text{FGA}}^\varepsilon\ _{L^2}$
$N = 1$	0.031445
$N = 2$	0.024814
$N = 4$	0.007579
$N = 8$	0.0018579
$\varepsilon = 1/256$	Error $\ \psi_0 - \psi_{\text{FGA}}^\varepsilon\ _{L^2}$
$N = 1$	0.030633
$N = 2$	0.024967
$N = 4$	0.0076045
$N = 8$	0.0018698
$\varepsilon = 1/512$	Error $\ \psi_0 - \psi_{\text{FGA}}^\varepsilon\ _{L^2}$
$N = 1$	0.030375
$N = 2$	0.025078
$N = 4$	0.0076103
$N = 8$	0.0018769

TABLE 2. L^2 error of $\psi_0(x) - \psi_{\text{FGA}}^\varepsilon(0, x)$ for Example 4.2. We display various values of ε and sum over N Bloch bands in $\psi_{\text{FGA}}^\varepsilon$.

Tables 1, and 2 show that FGA indeed matches the initial condition more closely as N increases. Furthermore, we have essentially the same L^2 error for each ε . This provides numerical verification of the independence of ε of the initial decomposition.

Remark. Let us note that from equation (1.4) the convergence rate should depend on the form of the lattice potential $V_\Gamma(x)$. Also, by equation (2.2), the convergence rate also depends on the form of the initial condition. We see from Examples 4.1, and 4.2 that the cosine lattice potential seem to produce faster convergence with respect to the number of bands used. Different initial conditions may also converge faster as N increases. Example 4.4 uses an initial condition projected onto the first band. Choosing such initial condition has the advantage of needing only to compute $\psi_{\text{FGA}}^\varepsilon$ over one band.

By examining the L^2 errors or the convergence rates, one could determine the minimum number of bands to sum over to achieve required accuracy. In Example 4.1, it shows that upon summing over $N = 4$ bands, the initial decomposition starts to resemble the initial condition.

4.2. Verification of the convergence rate of FGA. First, we choose to test the convergence rate of (2.9) with external potential $U(x) = 0$ in Examples 4.3 and 4.4. With this choice of potential, there is no need for a gauge-invariant algorithm. One can optimize the algorithm described in Section 3.2 by setting $\tilde{F}(t, q, p) = 1$ in (3.11) in Step 4. Thus, for Examples 4.3 and 4.4, numerical errors coming from $\tilde{F}(t, q, p)$ will be absent. Examples 4.5 and 4.6 have nonzero external potential so there will

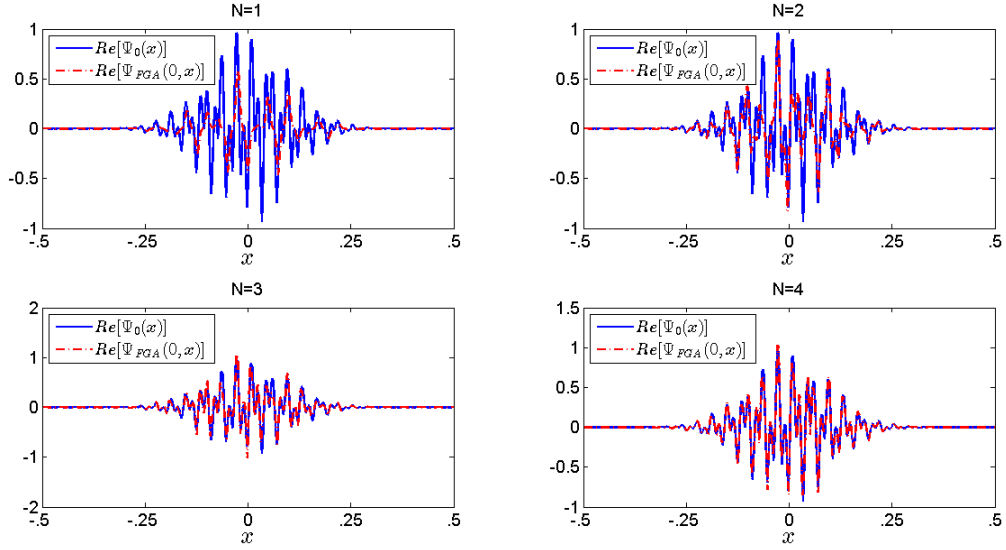


FIGURE 5. Initial decomposition for example 4.1. The real part of $\psi_0(x)$ and $\psi_{\text{FGA}}^\varepsilon(0, x)$ are shown for $\varepsilon = 1/256$. The summation in $\psi_{\text{FGA}}^\varepsilon(0, x)$ is over the first 4 lowest energy bands.

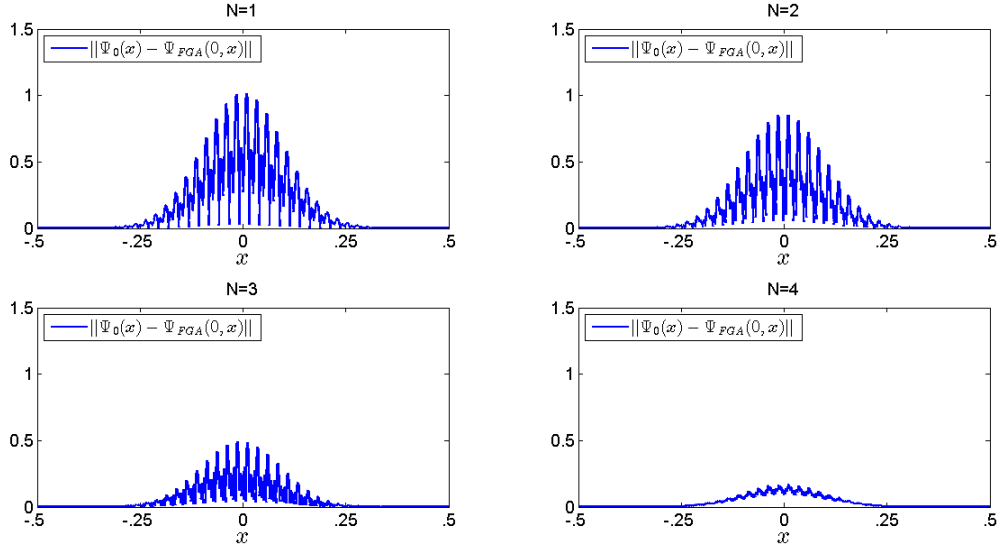


FIGURE 6. The plot of $\|\psi_0(x) - \psi_{\text{FGA}}^\varepsilon(0, x)\|_{l^2}$ for figure 5 is displayed here.

be some numerical errors introduced by $\tilde{F}(t, q, p)$. We continue using $2/\sqrt{\varepsilon}$ mesh points per unit interval in q and p and sum up to eight bands (except for Example 4.4). We choose a time step of size $\Delta t = T/150$. The exact solution to equation (1.1) will be computed using the Strang splitting spectral method [1]. For all of our examples, the Strang splitting spectral method did not need a mesh finer than $\Delta x = 1/2^{16}$ and $\Delta t = 1/2^{12}$.

	Error $\ \psi_{Spec} - \psi_{FGA}^\varepsilon\ _{L^2}$	Rate of Convergence
$\varepsilon = 1/8$	0.09112	
$\varepsilon = 1/16$	0.048907	0.8977
$\varepsilon = 1/32$	0.022603	1.1135
$\varepsilon = 1/64$	0.010555	1.0986

TABLE 3. L^2 error of $\psi_{Spec}(0.35, x) - \psi_{FGA}^\varepsilon(0.35, x)$ for various values of ε . The summation in ψ_{FGA}^ε is over the first 8 lowest energy bands.

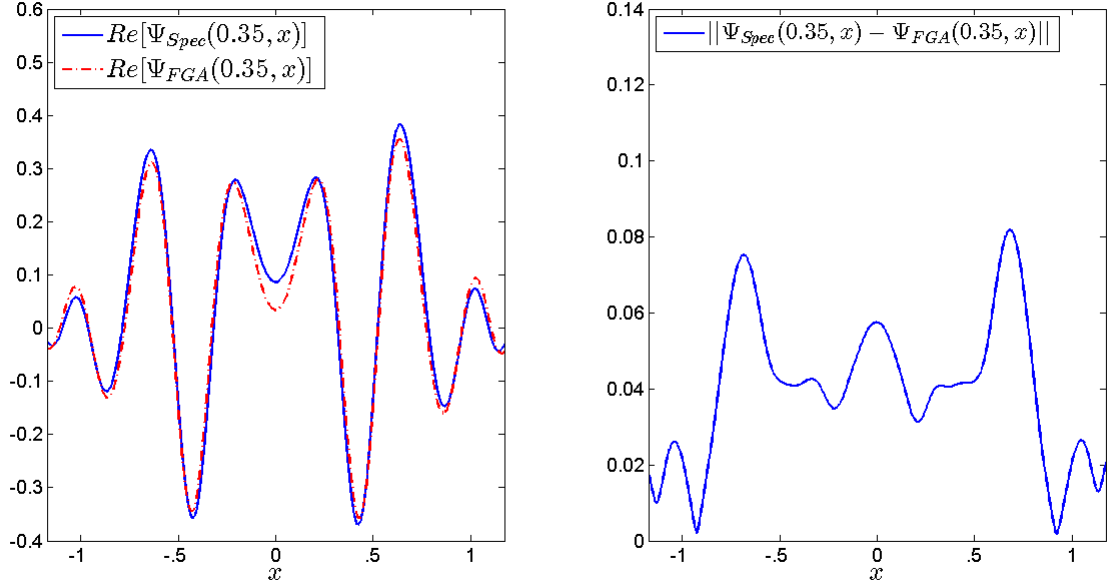


FIGURE 7. Example 4.3 plot of real parts of $\psi_{FGA}^\varepsilon(0.35, x)$ and $\psi_{Spec}(0.35, x)$ along side with the L^2 error for $\varepsilon = 1/8$.

Example 4.3. In this example we choose the initial condition to be $\psi_0 = A(x) \exp(iS(x)/\varepsilon)$ with $A(x) = \exp(-50x^2)$ and $S(x) = 0.3 + 0.1 \sin(x - 0.5)$. The exact solution is computed using the Strang Splitting spectral method. This is done at time $T = 0.35$. The lattice potential used is $V_\Gamma(x) = \cos(x)$. We record the data in Table 3. The convergence order of the data in table 3 is 1.0366. We display plots of the solution for $\varepsilon = 1/8, 1/16, 1/32$ and $1/64$ in Figures 7, 8, 9, and 10.

In the next example, we will choose initial condition projected onto one Bloch band. With this choice of initial condition, there will be no initial error.

Example 4.4. In this example we will choose an initial condition $\Pi_{n=1}^{\mathcal{W}, \varepsilon} \psi_0(x)$ given by (2.33) with $\psi_0(x) = A(x) \exp(iS(x)/\varepsilon)$ where $A(x) = \exp(-50x^2)$ and $S(x) = 0.3x + 0.1 \sin(x - 0.5)$ with lattice potential $\exp(-20x^2)$ and external potential $U(x) = 0$. We compute the solution at time $T = 0.35$ using the Strang Splitting spectral method and GIFGA. The L^2 errors are recorded in Table 4. The convergence order is 0.9814. We display plots of the solution for $\varepsilon = 1/64, 1/128$ and $1/256$ in Figures 11, 12, and 13.

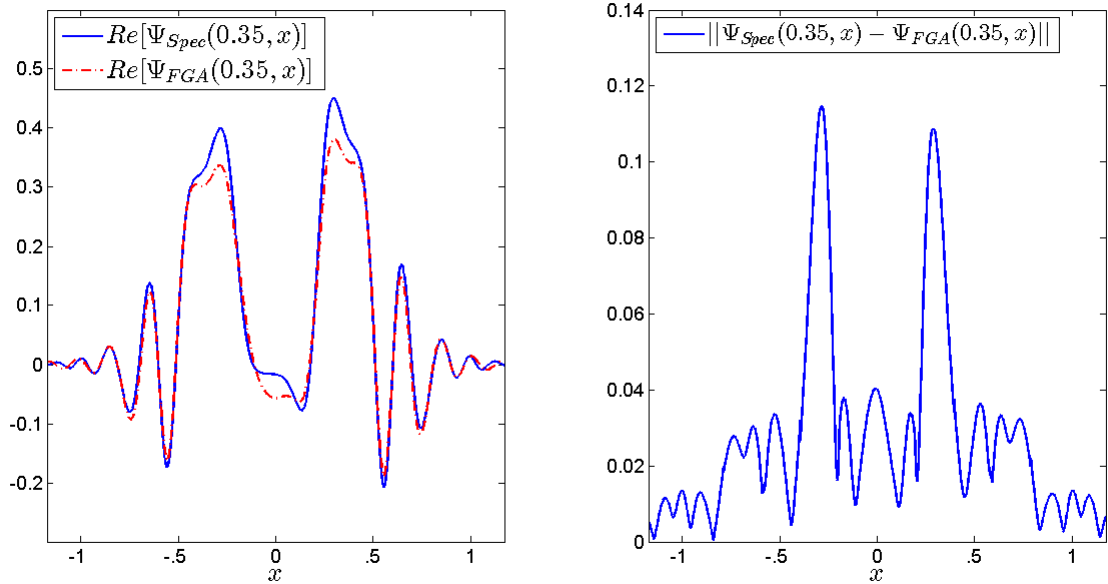


FIGURE 8. Example 4.3 plot of real parts of $\psi_{FGA}^\varepsilon(0.35, x)$ and $\psi_{Spec}(0.35, x)$ along side with the L^2 error for $\varepsilon = 1/16$.

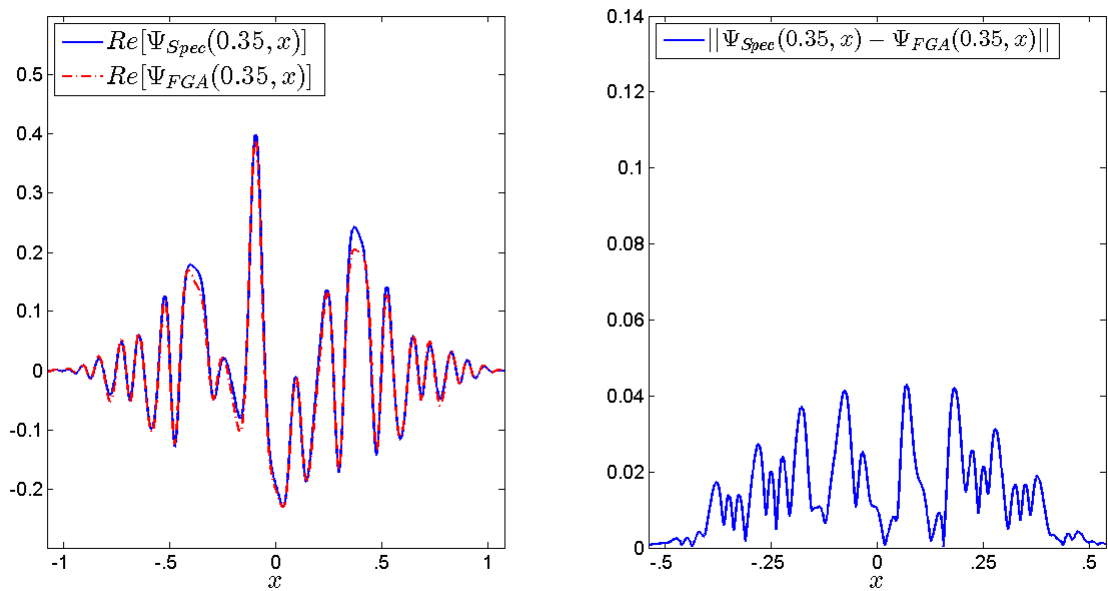


FIGURE 9. Example 4.3 plot of real parts of $\psi_{FGA}^\varepsilon(0.35, x)$ and $\psi_{Spec}(0.35, x)$ along side with the L^2 error for $\varepsilon = 1/32$.

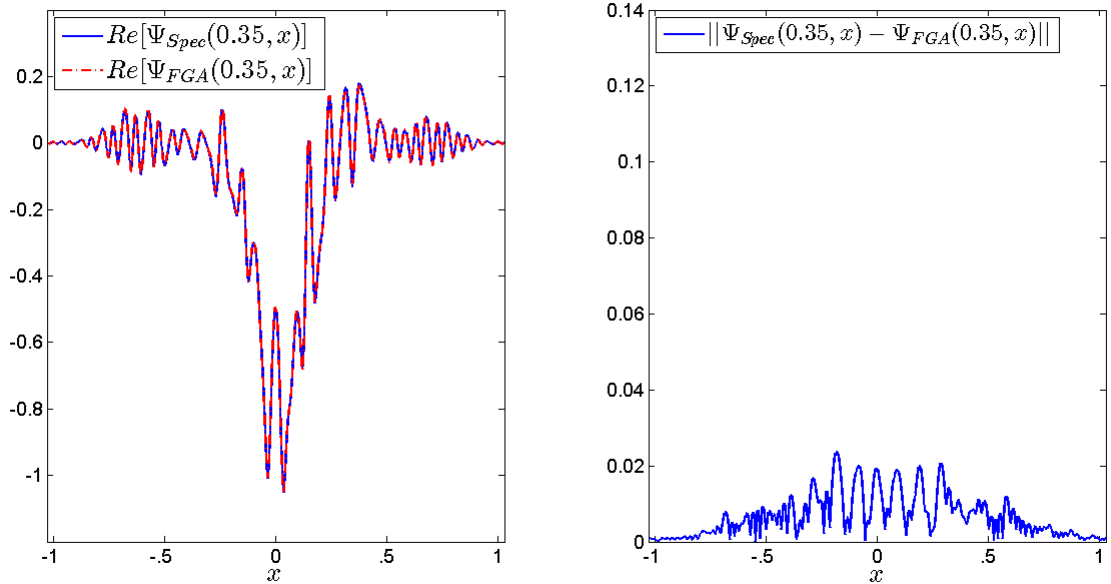


FIGURE 10. Example 4.3 plot of real parts of $\psi_{FGA}^\varepsilon(0.35, x)$ and $\psi_{Spec}(0.35, x)$ along side with the L^2 error for $\varepsilon = 1/64$.

	Error $\ \psi_{Spec} - \psi_{FGA}^\varepsilon\ _{L^2}$	Rate of convergence
$\varepsilon = 1/64$	0.0269	
$\varepsilon = 1/128$	0.0144	0.9015
$\varepsilon = 1/256$	0.0069	1.0614

TABLE 4. L^2 error of $\psi_{Spec}(0.35, x) - \psi_{FGA}^\varepsilon(0.35, x)$ for initial condition projected onto the first Bloch band.

Example 4.5. In this example we choose the initial condition to be $\psi_0 = A(x) \exp(iS(x)/\varepsilon)$ with $A(x) = \exp(-50x^2) \cos((x-0.5)/\varepsilon)$ and $S(x) = 0.3(x-0.5) + 0.1 \sin(x-0.5)$. The exact solution is computed using the Strang Splitting spectral method. This is done at time $T = 0.2$. The potential used is $V_\Gamma(x) = \exp(-25x^2)$ with external potential $U(x) = \frac{1}{2}x^2$. Our results are shown in Table 5. The convergence order of the data in table 5 is 0.9488. We display plots of the solution for $\varepsilon = 1/128, 1/256$ and $1/512$ in Figures 14, 15, and 16.

Example 4.6. In this example we choose the same initial condition as in Example 4.5. All of the same parameters as in Example 4.5 will also be used. The exact solution is again computed using the Strang Splitting spectral method at time $T = 0.2$. The only difference is that we change the external potential to $U(x) = \cos(x)$. The convergence order of the data in Table 6 is 0.8439. We display plots of the solution for $\varepsilon = 1/128, 1/256$ and $1/512$ in Figures 17, 18, and 19.

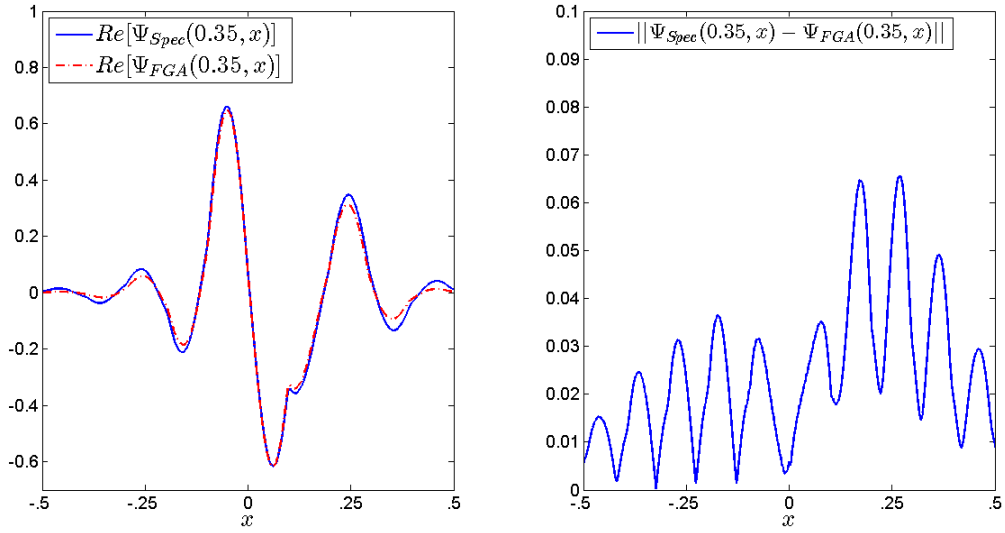


FIGURE 11. Example 4.4 plot of the real part of $\psi_{Spec}(0.35, x)$ and $\psi_{FGA}^\varepsilon(0.35, x)$ alongside with the L^2 error of $\psi_{Spec}(0.35, x) - \psi_{FGA}^\varepsilon(0.35, x)$ for example 4.4. We use $\varepsilon = 1/64$.

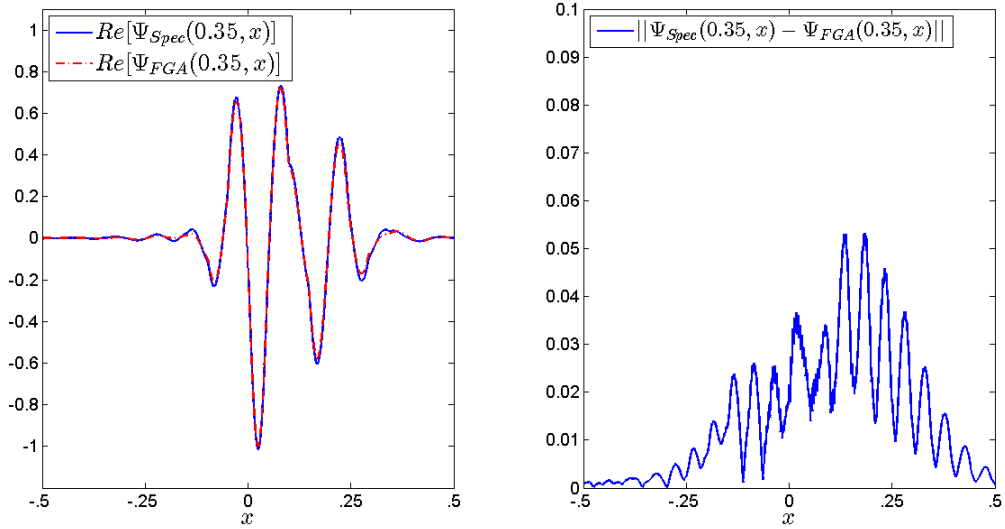


FIGURE 12. Example 4.4 plot of the real part of $\psi_{Spec}(0.35, x)$ and $\psi_{FGA}^\varepsilon(0.35, x)$ alongside with the L^2 error of $\psi_{Spec}(0.35, x) - \psi_{FGA}^\varepsilon(0.35, x)$ for example 4.4. We use $\varepsilon = 1/128$.

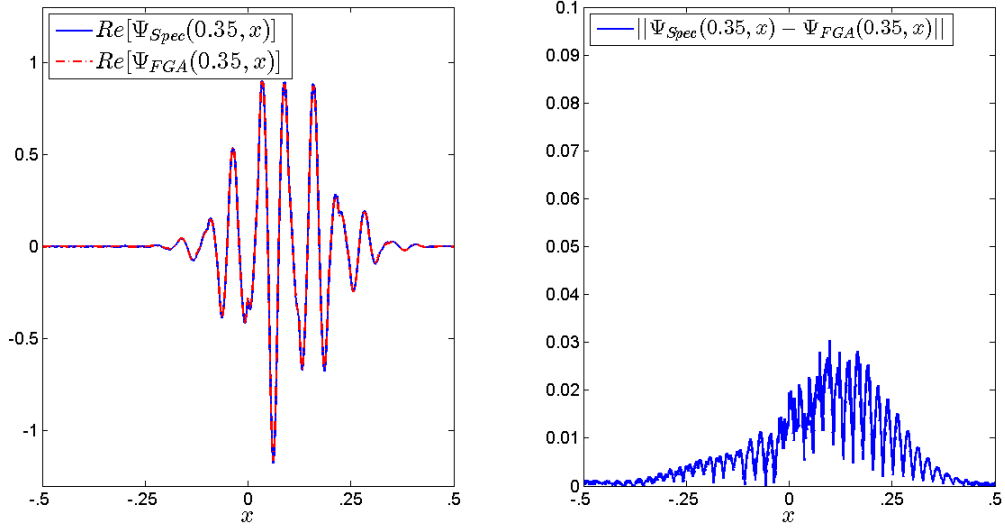


FIGURE 13. Example 4.4 plot of the real part of $\psi_{Spec}(0.35, x)$ and $\psi_{FGA}^\varepsilon(0.35, x)$ alongside with the L^2 error of $\psi_{Spec}(0.35, x) - \psi_{FGA}^\varepsilon(0.35, x)$ for example 4.4. We use $\varepsilon = 1/256$.

	Error $\ \psi_{Spec} - \psi_{FGA}\ _{L^2}$	Rate of Convergence
$\varepsilon = 1/64$	0.059576	
$\varepsilon = 1/128$	0.038811	.61826
$\varepsilon = 1/256$	0.015225	1.3500
$\varepsilon = 1/512$	0.0082833	0.8782

TABLE 5. L^2 error of $\psi_{Spec}(0.2, x) - \psi_{FGA}^\varepsilon(0.2, x)$ for various values of ε . The summation in ψ_{FGA}^ε is over the first 8 lowest energy bands.

	Error $\ \psi_{Spec} - \psi_{FGA}^\varepsilon\ _{L^2}$	Rate of Convergence
$\varepsilon = 1/128$	0.039714	
$\varepsilon = 1/256$	0.019057	1.0593
$\varepsilon = 1/512$	0.012327	0.6285

TABLE 6. L^2 error of $\psi_{Spec}(0.2, x) - \psi_{FGA}^\varepsilon(0.2, x)$ for various values of ε . The summation in ψ_{FGA}^ε is over the first 8 lowest energy bands.

5. DISCUSSION AND CONCLUSION

In this paper, we generalize the Herman-Kluk propagator for the linear Schrödinger equation (LSE), and develop the gauge-invariant frozen Gaussian approximation method for LSE with periodic potentials in the semiclassical regime. The method is invariant with respect to the gauge choice of the Bloch eigenfunctions, and thus avoids the numerical difficulty of computing gauge-dependent Berry phase. The numerical examples show that that the frozen Gaussian approximation is indeed a good

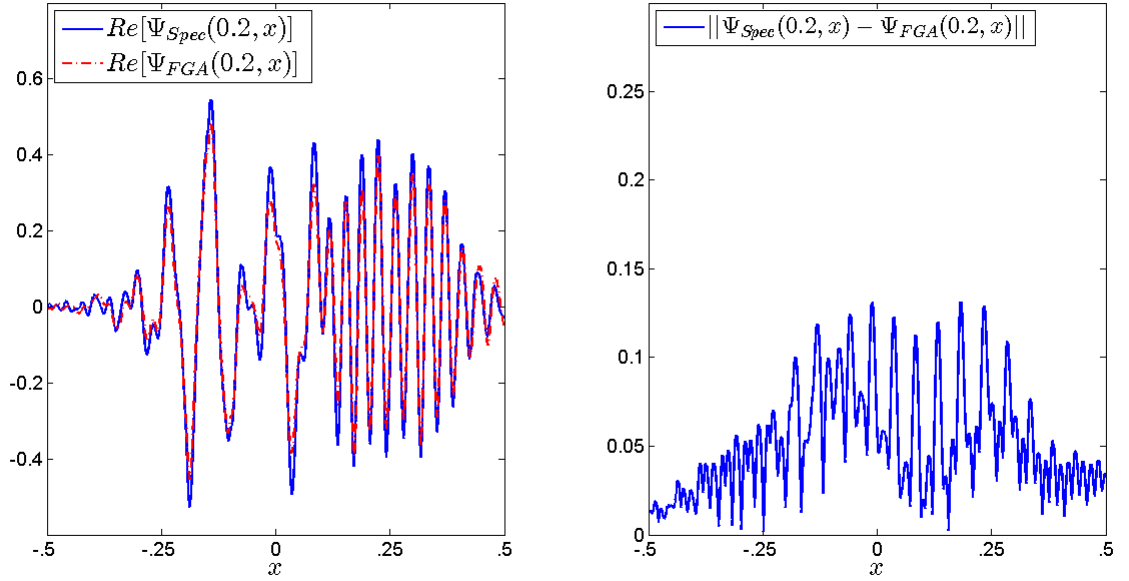


FIGURE 14. Example 4.5 plot of the real parts of $\psi_{FGA}^\varepsilon(0.2, x)$ and $\psi_{Spec}(0.2, x)$ along side with the L^2 error for $\varepsilon = 1/128$.

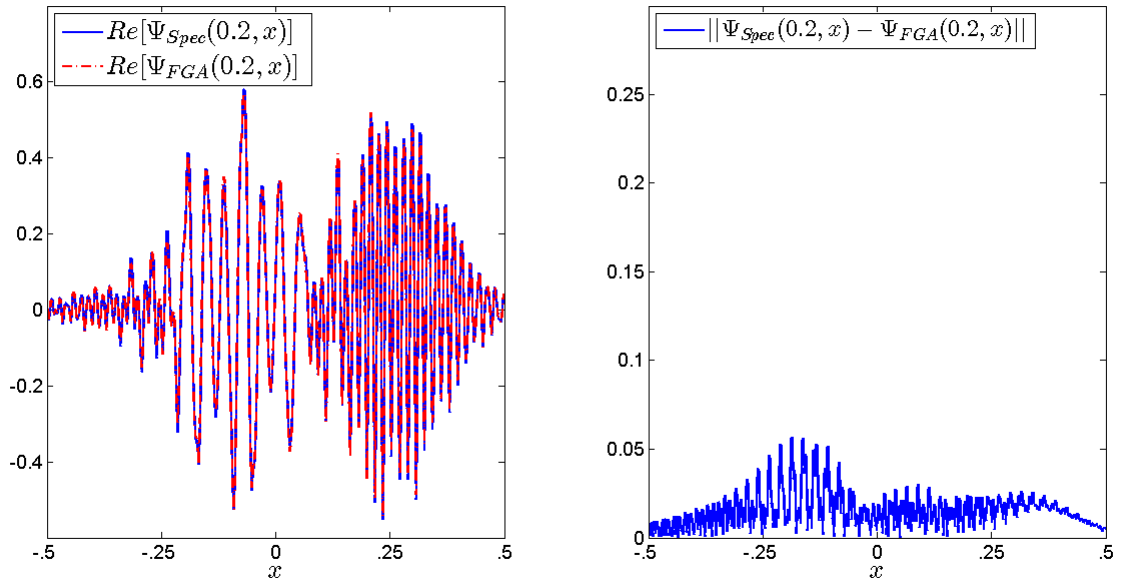


FIGURE 15. Example 4.5 plot of the real parts of $\psi_{FGA}^\varepsilon(0.2, x)$ and $\psi_{Spec}(0.2, x)$ along side with the L^2 error for $\varepsilon = 1/256$.

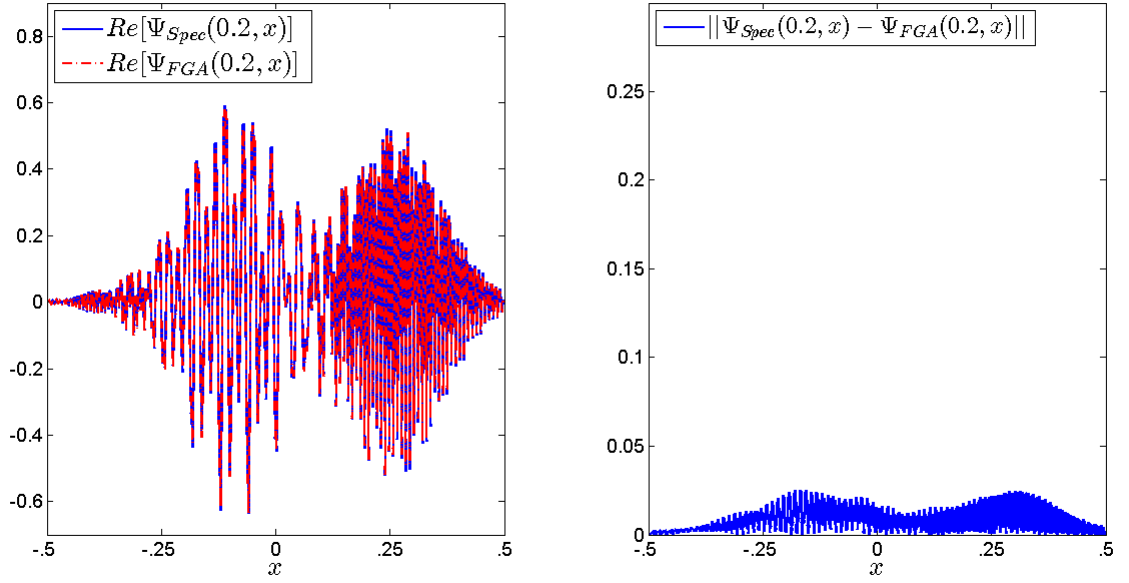


FIGURE 16. Example 4.5 plot of the real parts of $\psi_{FGA}^\varepsilon(0.2, x)$ and $\psi_{Spec}(0.2, x)$ along side with the L^2 error for $\varepsilon = 1/512$.

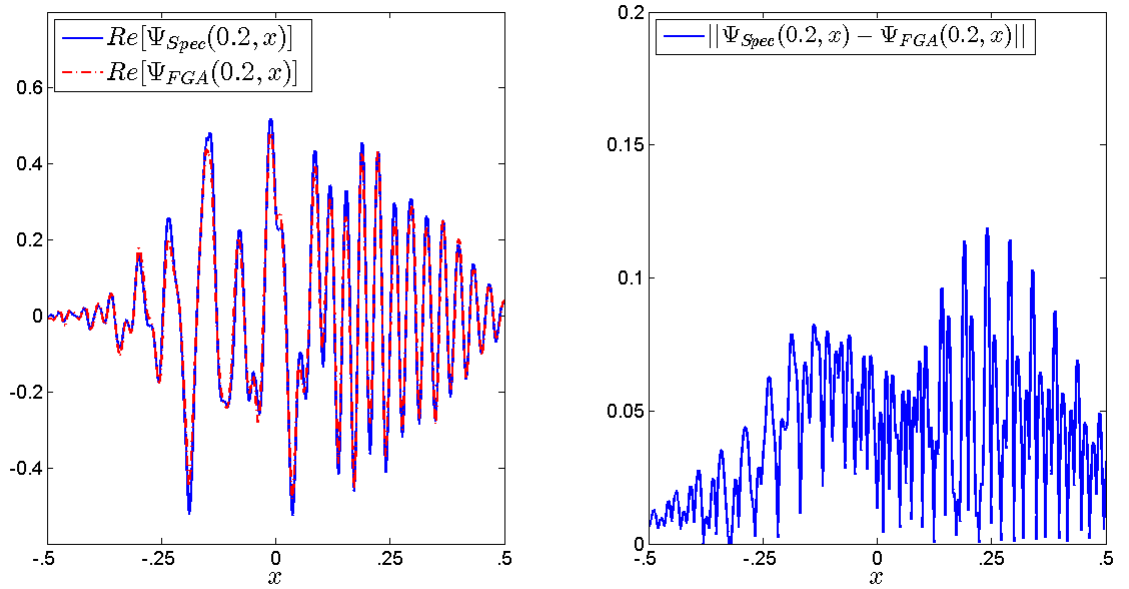


FIGURE 17. Plot of real parts of $\psi_{FGA}^\varepsilon(0.2, x)$ and $\psi_{Spec}(0.2, x)$ along side with the L^2 error for $\varepsilon = 1/128$.

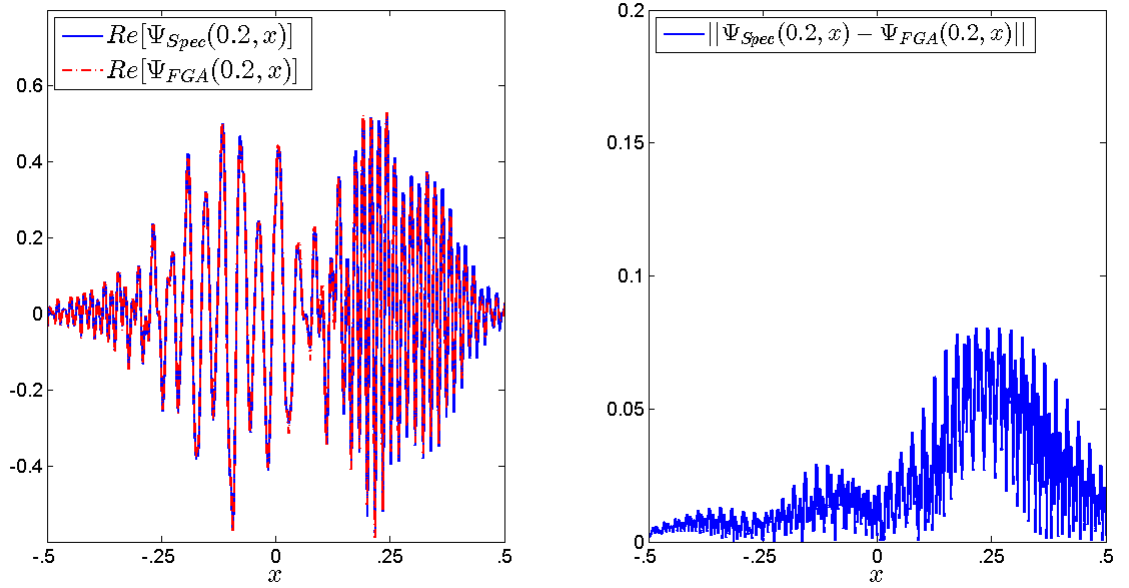


FIGURE 18. Plot of real parts of $\psi_{FGA}^\varepsilon(0.2, x)$ and $\psi_{Spec}(0.2, x)$ along side with the L^2 error for $\varepsilon = 1/256$.

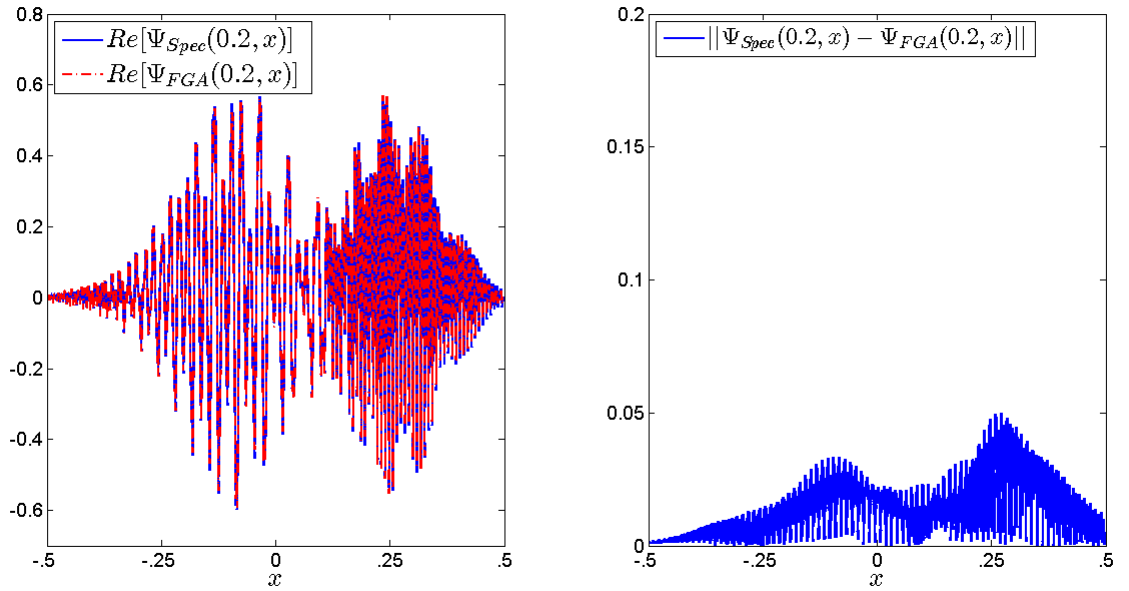


FIGURE 19. Plot of real parts of $\psi_{FGA}^\varepsilon(0.2, x)$ and $\psi_{Spec}(0.2, x)$ along side with the L^2 error for $\varepsilon = 1/512$.

approximation to the exact solution of the Schrödinger equation (1.1) for $\varepsilon \ll 1$. The convergence order of our numerical results confirms the estimate given in [3]

$$(5.1) \quad \|\psi_{Exact}^\varepsilon(t, x) - \psi_{FGA}^\varepsilon(t, x)\|_{L^2} = \mathcal{O}(\varepsilon).$$

In future, we will study high dimensional examples where band-crossing happens quite common, and thus requires more techniques than the scope of this paper.

REFERENCES

- [1] W. Bao, S. Jin, and P.A. Markowich, *On time-splitting spectral approximations for the Schrödinger equation in the semiclassical regime*, J. Comput. Phys. **175** (2002), 487–524.
- [2] A. Bensoussan, J.L. Lions, and G. Papanicolaou, *Asymptotic analysis for periodic structures*, North-Holland Publishing Co., Amsterdam-New York, 1978.
- [3] R. Delgadillo, J. Lu, and X. Yang, *Frozen Gaussian approximation for high frequency wave propagation in periodic media*, 2015. preprint, arXiv:1504.08051.
- [4] M. Dimassi, J.C. Guillot, and J. Ralston, *Gaussian beam construction for adiabatic perturbations*, Math. Phys. Anal. Geom. **9** (2006), 187–201.
- [5] E. J. Heller, *Cellular dynamics: a new semiclassical approach to timedependent quantum mechanics*, J. Chem. Phys. **94** (1991), 2723–2729.
- [6] E.J. Heller, *Frozen Gaussians: A very simple semiclassical approximation*, J. Chem. Phys. **75** (1981), 2923–2931.
- [7] M.F. Herman and E. Kluk, *A semiclassical justification for the use of non-spreading wavepackets in dynamics calculations*, Chem. Phys. **91** (1984), 27–34.
- [8] Z. Huang, S. Jin, P.A. Markowich, and C. Sparber, *A Bloch decomposition-based split-step pseudospectral method for quantum dynamics with periodic potentials*, SIAM J. Sci. Comput. **29** (2007), 515–538.
- [9] ———, *Numerical simulation of the nonlinear Schrödinger equation with multi-dimensional periodic potentials*, Multiscale Model. Simul. **7** (2008), 539–564.
- [10] ———, *On the Bloch decomposition based spectral method for wave propagation in periodic media*, Wave Motion **46** (2009), 15–28.
- [11] L. Jefferis and S. Jin, *A Gaussian beam method for high frequency solution of symmetric hyperbolic systems with polarized waves*, 2014. preprint.
- [12] S. Jin, P.A. Markowich, and C. Sparber, *Mathematical and computational methods for semiclassical Schrödinger equations*, Acta Numer. **20** (2011), 211–289.
- [13] S. Jin, H. Wu, and X. Yang, *Gaussian beam methods for the Schrödinger equation in the semi-classical regime: Lagrangian and Eulerian formulations*, Commun. Math. Sci. **6** (2008), 995–1020.
- [14] S. Jin, H. Wu, X. Yang, and Z. Huang, *Bloch decomposition-based Gaussian beam method for the Schrödinger equation with periodic potentials*, J. Comput. Phys. **229** (2010), 4869–4883.
- [15] R. D. King-Smith and David Vanderbilt, *Theory of polarization of crystalline solids*, Phys. Rev. B **47** (1993Jan), 1651–1654.
- [16] J. Lu and X. Yang, *Frozen Gaussian approximation for high frequency wave propagation*, Commun. Math. Sci. **9** (2011), 663–683.
- [17] ———, *Convergence of frozen Gaussian approximation for high frequency wave propagation*, Comm. Pure Appl. Math. **65** (2012), 759–789.
- [18] ———, *Frozen Gaussian approximation for general linear strictly hyperbolic system: Formulation and Eulerian methods*, Multiscale Model. Simul. **10** (2012), 451–472.
- [19] M. Motamed and O. Runborg, *Taylor expansion and discretization errors in Gaussian beam superposition*, Wave Motion **47** (2010), 421–439.
- [20] J. Qian and L. Ying, *Fast Gaussian wavepacket transforms and Gaussian beams for the Schrödinger equation*, J. Comput. Phys. **229** (2010), 7848–7873.
- [21] ———, *Fast multiscale Gaussian wavepacket transforms and multiscale Gaussian beams for the wave equation*, Multiscale Model. Simul. **8** (2010), 1803–1837.
- [22] M. Reed and B. Simon, *Methods of modern mathematical physics, Vol IV*, Academic Press, New York, 1980.

- [23] G. Sun, *A simple way constructing symplectic Runge-Kutta methods*, Math. Comp. **18** (2000), 61–68.
- [24] H. Wu, Z. Huang, S. Jin, and D. Yin, *Gaussian beam methods for the Dirac equation in the semi-classical regime*, 2012. preprint.
- [25] D. Yin and C. Zheng, *Gaussian beam formulations and interface conditions for the one-dimensional linear Schrödinger equation*, Wave Motion **48** (2011), 310–324.

DEPARTMENT OF MATHEMATICS, UNIVERSITY OF CALIFORNIA, SANTA BARBARA, CA 93106

E-mail address: rdelgadi@math.ucsb.edu

DEPARTMENTS OF MATHEMATICS, PHYSICS, AND CHEMISTRY, DUKE UNIVERSITY, BOX 90320, DURHAM, NC 27708

E-mail address: jianfeng@math.duke.edu

DEPARTMENT OF MATHEMATICS, UNIVERSITY OF CALIFORNIA, SANTA BARBARA, CA 93106

E-mail address: xuyang@math.ucsb.edu